SYNTHESIS AND CHARACTERIZATION OF MAGNETIC NANOPARTICLES TO INCORPORATE INTO SILICON WAVEGUIDES TO BE USED AS OPTICAL ISOLATORS

SYNTHESIS AND CHARACTERIZATION OF MAGNETIC NANOPARTICLES TO INCORPORATE INTO SILICON WAVEGUIDES TO BE USED AS OPTICAL ISOLATORS

By: Amr Ibrahim, B. ENG.

A THESIS SUBMITTED TO THE DEPARTMENT OF ENGINEERING PHYSICS AND THE SCHOOL OF GRADUATE STUDIES OF MCMASTER UNIVERSITY IN PARTIAL FULFILMENT OF THE REQUIREMENTS FOR THE DEGREE OF MASTER OF APPLIED SCIENCE

McMaster University Master of Applied Science (2019) Hamilton, Ontario (Engineering Physics)

AUTHOR: Amr Ibrahim, B.Eng. (McMaster University, Hamilton, Ontario)

SUPERVISOR: Dr. Ayse Z. Turak

NUMBER OF PAGES: Viii, 88

Abstract

Integrated optical isolators will become necessary as optical networks continue to grow and the need for monolithic integration and greater functionality increases. The use of magnetic nanoparticles as Faraday rotators to achieve isolation has been widely researched and reported. Therefore, magnetic nanoparticles are of particular interest.

Magnetic γ - Fe_2O_3 and SnO_2 nanoparticles were synthesized using the diblock copolymer reverse micelles method. The processes were shown in detail with the aid of Raman spectroscopy to reveal the iron oxide evolution. Moreover, the magnetic properties of the nanoparticles were evaluated by superconducting quantum interference device (SQUID) magnetometer. Using a low temperature annealing process, we showed that higher percentage of γ-Fe_2O_3 phase was produced and could be incorporated in practical devices. One practical use is to be used as Faraday rotators in an optical isolator.

The size of the nanoparticles can be changed simply by changing the loading ratio of $FeCl_3$ or using different polymers to yield different sizes of the nanoparticles. The size and dispersion of the nanoparticles were determined using atomic force microscopy (AFM-QNM) and scanning electron microscope (SEM). With a good control in terms of size and dispersion, the magnetic γ-Fe_2O_3 were employed on silicon waveguides to test for optical isolation. The results showed no optical isolation from the γ-Fe_2O_3 nanoparticles; this is likely due to the modal phase mismatch between the cladding and the nanoparticles. With a few changes in the design of the waveguides and dropping of the nanoparticles; we can have a fully functional integrated optical isolator on silicon.

Contents

List of Figures

Chapter 1

Introduction

Extensive research in microphotonics has led to it surpassing electronics in terms of bandwidth distance product and power consumption for telecom and datacom applications(1). In the applications for telecommunications, some optical feedback in lasers and optical amplifiers cause noise and instabilities in lasers(2,3). This feedback is mainly caused by back reflections from the optical fiber at the laser output. The effect of the reflecting fiber facet is to create a double cavity state in the laser if the phase coherence is maintained, or act as an external light source if the coherence is lost. Fluctuations in laser intensity and frequency for both the double cavity and external light source state will exist. For the external light source, the fluctuations come from the random generation of locking and unlocking states from the frequency changes which is caused by the temperature variations of the laser diode. On the other hand, for the double cavity state the fluctuations are mainly caused by the mechanical vibrations of the fiber which change the length from the reflection point to the cavity creating phase variations. In both cases, the intensity and frequency noise are both directly proportional to the effective reflectivity of the fiber. The reflectivity commonly refers to the amount of reflected power from the fiber that returns to the laser cavity(2,3). In order to effectively reduce the reflectivity, an isolator is placed in front of the laser. The isolator will block the back-reflected light, thus readily reducing the intensity and frequency fluctuations.

Optical isolators are therefore important components in lasers and optical amplifiers(2,4). The main function is to eliminate noise caused by back-reflections into the lasers and amplifiers. The continued growth of telecommunication networks makes it a necessity to have an integrated system where the optical isolators are monolithically integrated on the same chip as lasers and/or amplifiers. The monolithic integration of the isolators will allow us to reduce costs and increase functionality of our devices.

Optical isolators only allow light to propagate in one direction, utilizing a non-reciprocal phenomenon which is Faraday rotation. Faraday rotation is non-reciprocal in the idea that the rotation is not dependent on the direction of light propagation. If light propagates through a Faraday rotating medium, after a single pass the polarization is rotated by an angle θ, after a round-trip the polarization is rotated by an angle of 2θ. Therefore, effectively stopping back-reflections of light.

The magneto-optical effect is the change in the propagation of an electromagnetic wave through a medium by the presence of a quasistatic magnetic field. An example of the magneto-optical effect is Faraday rotation, which is an interaction between light and a magnetic field in a medium. The Faraday effect causes a rotation of the plane of polarization which is linearly proportional to the component of the magnetic field in the direction of propagation of light (5).

In the last 20 years, ongoing research has been able to show that nanoparticles with sufficient magnetic response show enhanced Faraday rotation, including Fe_2O_3 nanoparticles (6). The enhancement in Faraday rotation is allowed in such material due to the composition of the material and the particles' arrangement more specifically the saturation magnetization and coercive field. Several authors were able to experimentally and theoretically calculate the required size of the nanoparticles while showing an enhancement in Faraday rotation (39).

Using the concept of Faraday rotation aiming for nanoparticles synthesis with high saturation magnetization and coercive field, we can produce iron oxide and tin oxide nanoparticles with the proper dispersion and magnetization that should have a high Faraday rotation. This can be therefore integrated into optical systems, where the nanoparticles should switch light polarization, allowing light to travel in one direction decreasing scattering.

The main focus of this thesis is on the synthesis and deposition of magnetic nanoparticles onto silicon waveguides in a controlled manner. In order to accomplish this goal, diblock copolymer reverse micelles synthesis procedure has been applied in the nanoparticle production. The process of the magnetic nanoparticles is explained in detail in chapters 4 and 6 for iron oxide and tin oxide respectively. The composition, crystal structure and magnetic properties of monolayer iron oxide nanoparticles and tin oxide nanoparticles are investigated using a variety of characterization techniques in chapters 5 for iron oxide and 6 for tin oxide. The preliminary results from integrating the nanoparticles onto the silicon waveguides are shown in chapter 7. The full experimental procedures are explained in detail in chapter 3.

Chapter 2

Background and motivation

2.1. Magnetic nanoparticles

Recent research in the last 30 years has been heavily focused on magnetic nanoparticles. The heavy research has been ongoing due to the interesting magnetization of small particles and clusters, as well as, the high interest expressed by different industries which has yielded a lot of different applications in the biomedical field and in the electronics field including high density data storage disks(7,8), high-density data storage disks(9), Li-ion batteries(10), drug delivery systems(11), and magnetic resonance imaging(12,13). In recent years as internet traffic has been explosively growing, the use of magnetic nanoparticles has been incorporated into the integrated optics field(4,14). In practice, the magnetic properties of the nanoparticles are directly related to their crystal structure and size for all the different applications.

2.1.1 FeO_x Crystal structure

Iron oxide nanoparticles varying in diameter between 1 and 100 nanometers have attracted much attention due to their fine magnetic properties and massive field of applications. The most common iron oxides that are used are: magnetite (Fe_3O_4), maghemite ($\gamma - Fe_2O_3$) and hematite (α - Fe_2O_3). The magnetic properties of the particles is directly related to the crystallinity of the nanoparticles, as the arrangement between the Fe and O atoms control the magnetic dipole arrangement(15). Iron oxide is interesting as it is possible to have different phases with different crystallographic structures existing. Table 1 shows the physical properties for the iron oxides.

Table 1.1. Physical properties of the iron oxide nanoparticles (11).

Properties	Magnetite	Maghemite	Hematite
Formula	Fe_3O_4	$\gamma - Fe_2O_3$	α - Fe_2O_3
Structure type	Inverse Spinel	Defect Spinel	Corundum
Crystallographic system	Cubic	Cubic	Hexagonal
Anion Stacking	FCC (111)	FCC (111)	HCP (001)
Magnetism	Ferri-	Ferri-	Weak Ferro- /Anti
Curie temperature (T_c)	850	820-986	956

Magnetite (Fe_3O_4) is a black magnetic mineral which is also called iron (II, III) oxide or ferrous ferrite. It exhibits a strong magnetic response(16). Maghemite ($\gamma - Fe_2O_3$) is a brown magnetic mineral, which naturally occurs in soils. It exhibits strong magnetism and it is metastable with respect to hematite. Hematite (α - Fe_2O_3) has a reddish-brown color and is one of the main ores of iron. Hematite is an antiferromagnetic magnetic material below the Moin transition at 250K and is weakly ferromagnetic above the Morin transition and below its Neel temperature at 948K(16).

Moreover, hematite has a corundum structure while Maghemite has an inverse spinel structure. The magnetic properties of spinels are sensitive to the type of cations and their distribution among the two interstitial sites of spinel lattice. The non-magnetic phase transition of Fe_3O_4 nanoparticles (from $\gamma - Fe_2O_3$ to α - Fe_2O_3) occurs at about 585°C (17). There have been a few studies done on high temperature phase transition in ferrites(18–20). Both hematite and maghemite phases are present in nature, while other phases such as the $\beta - Fe_2O_3$ with bixbyite structure and $\varepsilon - Fe_2O_3$ with orthorhombic structure are rare phases only produced in the laboratory (16). Figure 2.1 shows the different crystal structures of the iron oxide(21).

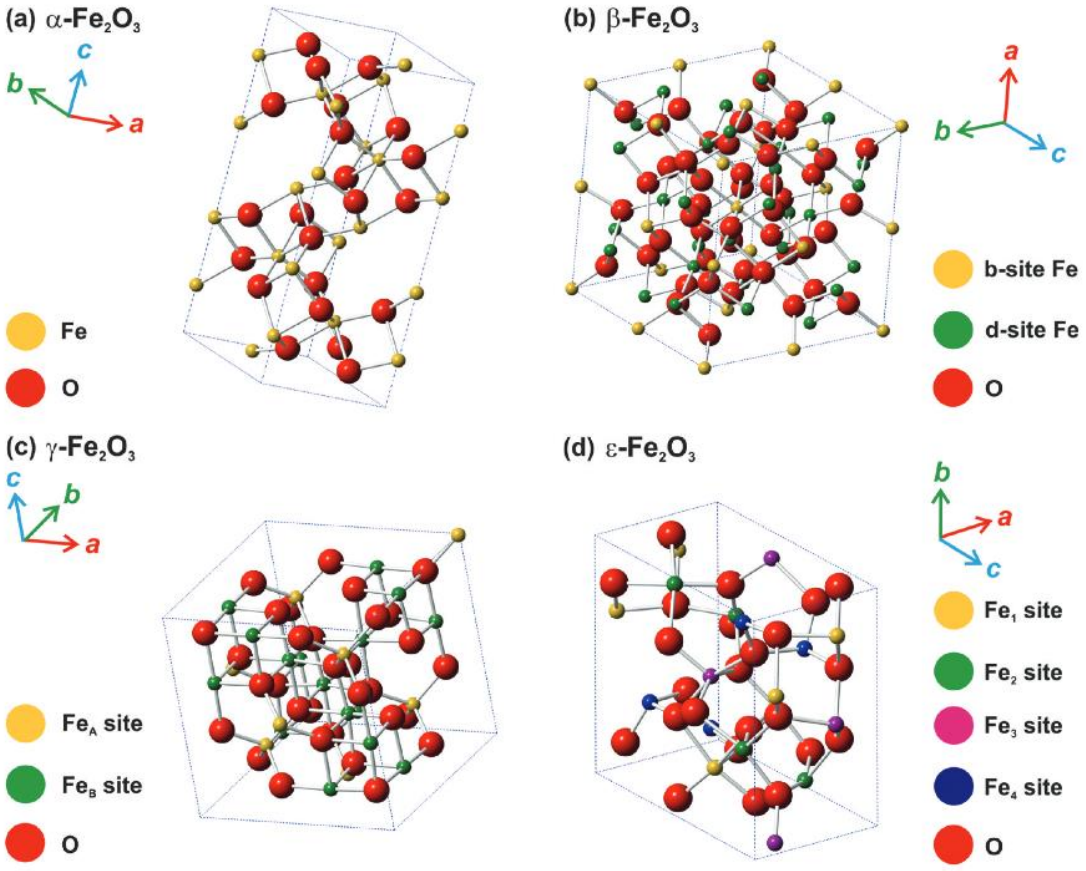

Figure 2.1. Representation of the fundamental crystal structure of Fe_2O_3(21): (a) α-Fe_2O_3 (b)β-Fe_2O_3 (c) γ- Fe_2O_3 (d)ϵ- Fe_2O_3

Maghemite is of particular interest in practical applications owing to its high Curie temperature (T_c = 928K), with relatively high ferrimagnetism at room temperature, and stability against oxidation(16) particularly used as a contrast agents for magnetic resonance imaging (MRI). Hematite is a very weak ferrimagnet but is a more thermodynamically stable phase. As a result, it is necessary to prevent its formation to achieve nanoparticles with significant magnetic properties. Iron oxide nanoparticles can be synthesized by a variety of different techniques such as polyol process(22), sol gel process(23), reverse micelles(24,25), precipitation route(26), sonochemical synthesis(27) and microemulsion technique(28).

2.1.2. SnOx Crystal structure

Tin oxide is a semiconductor material, transparent, and of high chemical and mechanical stability. Tin oxide has multiple room temperature phases such as the rutile-type SnO_2, tetragonal SnO and Sn_3O_4. However, we are interested in stannic dioxide (SnO_2). The SnO_2 is an important semiconductor having a wide bandgap energy in the range of 3.6 eV and 3.9 eV (29). SnO_2 is an n-type semiconductor in its purest ground state. The crystal structure is presented in the figure below. This crystalline structure contains metal atoms in octahedral coordination and oxygen in planar three-coordination. Tin dioxide has been widely studied for its distinctive property such as excellent optical, electrical, great thermal stability and chemical property(30). Different methods have been used to fabricate stannic dioxide nanoparticles which include spray prolysis (31), hydrothermal (17), evaporation tin grains in air (32), chemical vapor deposition (33), thermal evaporation of SnO_2 powders (34) and the sol-gel method (35). The SnO_2 have several applications in solar cells, in lithium batteries, gas sensors, and as a catalyst and glass electrodes (36).

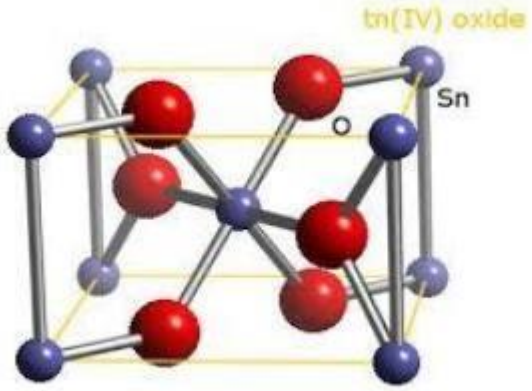

Figure 2.2. Crystal structure of SnO_2(16)

Room temperature ferromagnetism has been reported in SnO_2 in room temperature by many groups (37,38), as well as, metal doped semiconductor oxides (39–41).

2.2. Magnetic properties

The magnetic moment is a quantitative measure of the magnetic strength and the orientation of a magnet or an object that produces a magnetic field. As figure 2.3 shows, in the paramagnetic state the magnetic moments of atoms are randomly oriented, meaning the crystal has a zero net magnetic moment. The atomic magnetic moments partially align when an external magnetic field is applied in the direction of the field resulting in a positive net magnetic moment, while having no magnetic moment when the field is removed. In a ferromagnetic crystal, the magnetic moments are aligned even without an applied external magnetic field. This parallel alignment of the magnetic moments results in a large net magnetization even in the absence of a magnetic field.

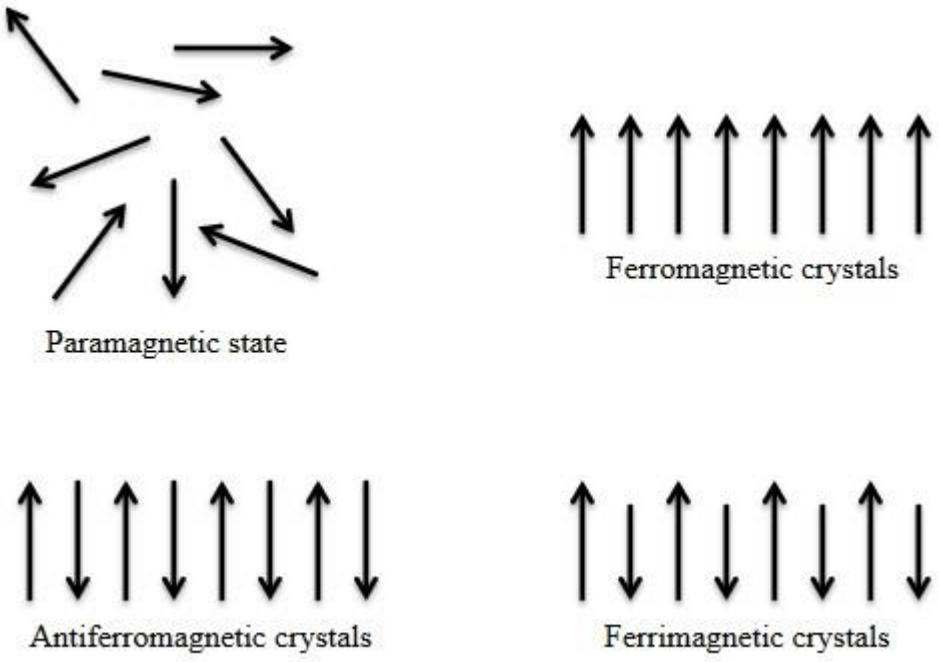

Figure 2.3. The magnetic spin alignments in different types of crystals.

However, in a ferrimagnetic crystal, two types of atoms with different magnetic moments are aligned in an antiparallel fashion with different magnitudes. This difference in magnitudes

creates a net magnetic moment. The crystal is antiferromagnetic if the antiparallel moments have the same magnitudes. Antiferromagnetic material has a net magnetic moment of zero.

The magnetization (M) is a representative of the net magnetic moment per unit volume aligned in parallel to the external magnetic field. Typically, the magnetic domains existing in a crystal have different alignments as figure 2.4 shows causing the magnetization in a crystal to be lower as the magnetic moments are not aligning perfectly so the magnetization decreases.

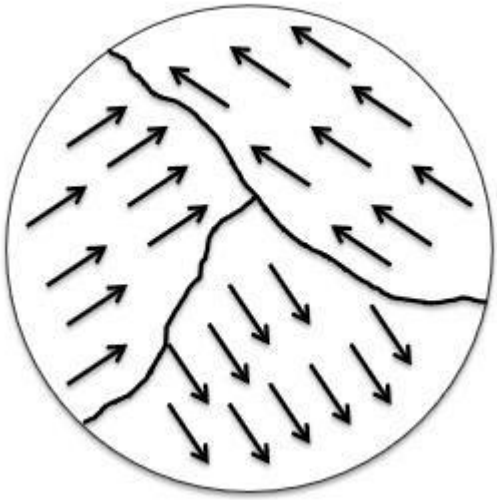

Figure 2.4. The magnetic domains in a crystal (42).

When an external magnetic field (H) is applied to a crystal, the crystal will have a magnetization (M). The magnetization of the crystals increases with the increase in the applied external magnetic field, till the magnetization hits the maximum value called the saturation magnetization (M_s). As the field is removed, the magnetization has a nonzero value which is generally referred to as the remnant magnetization (M_r).

In order to bring the magnetization back to zero, a coercivity field (H_c) must be applied in an antiparallel fashion. This process is shown in figure 2.5 which is known as the hysteresis loop.

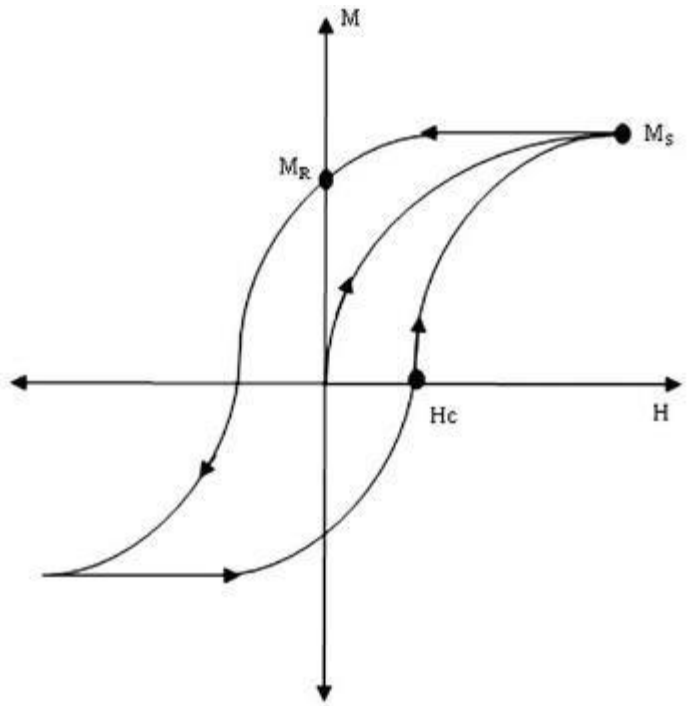

Figure 2.5. The Hysteresis loop. Representation of the typical magnetization curve for ferromagnetic and ferrimagnetic materials (30).

As the size of the crystal decreases, the number of domains decreases as well. The crystal can become a single domain when the size is below a critical value. This is interesting as a single domain magnetic crystal has no hysteresis loop; it is superparamagnetic. This means that the crystal will demagnetize completely (M=0) as the field is removed.

Moreover, the alignment of the magnetic moments is a function of temperature. As the temperature increases, the alignment then starts to be more disordered and beyond a certain critical temperature, the magnetization will then become zero. This critical temperature is called the Curie temperature (T_c).

The magnetic properties for iron oxide nanoparticles can be attributed to the fact that Iron atoms have four unpaired electrons in 3d orbital, so it has a strong magnetic moment. Fe^{3+} ions have five unpaired electrons in 3d orbital, and Fe^{2+} ions, they can be in ferromagnetic, antiferromagnetic or ferrimagnetic states (11). Moreover, room temperature ferromagnetism has been reported in undoped SnO_2 nanosystems(37). Authors(43,44) were able to prove theoretically and experimentally that the main reason behind the observed ferromagnetism in SnO_2 system is the presence of Sn^{4+} vacancy. The vacancies are the main source of magnetism in SnO_2 systems.

Sundaresan et al. (43) were able to show the nanoparticles of metal oxides such as CeO_2, Al_2O_3, ZnO, and SnO_2 exhibit room-temperature ferromagnetism that the bulk oxides don't exhibit, as they exhibit diamagnetism.

2.2.2. Size control for a single domain crystal

Typically, the size of the nanoparticles affects the magnetic response of said particles. Usually, the size of the particles vary but is in the range of 7 – 30 nm, which is smaller than the size of a single domain. Therefore, the magnetic moments in a particle are perfectly aligned, which means it is fully magnetized (30). To calculate the single domain critical diameter, we use the following equation (45,46):

$$D_{single} \sim 36 \frac{\sqrt{A * K_{eff}}}{\mu_0 * {M_s}^2}$$

Where, A is the exchange constant, K_{eff} is the effective anisotropy constant, μ_0 is the vacuum permeability and M_s is the saturation magnetization. The nanoparticles above this limit are aligned in different directions, however, below this limit the particles would be magnetized such that the magnetic moments of the atoms are aligned in one direction. The typical values for the γ – Fe_2O_3 are (32):

A is in the order of 10^{-11} J/m

K_{eff} is on the order of 4 – 8 x10^3 J/m^3

M_s is typically around 350 emu/cm^3

These values for γ – Fe_2O_3 yield a low limit for the diameter below which the particles are single domain to be around 50 nm.

Similarly, for tin oxide the typical values for the SnO_2 are (47,48):

A is in the order of 10^{-12} J/m

K_{eff} is on the order of 5 – 9 x10^3 J/m^3

M_s is typically around 250-300 emu/cm^3

These values for SnO_2 yield a low limit for the diameter below which the particles are single domain to be around 45 nm.

Figure 2.6 shows the effects of having single domain nanoparticles in the ferromagnetic region where the coercivity is highest in the ferromagnetic region, decreases as we get into the multi-domain region and is zero in the super-paramagnetic limit. This is important as we want to hit that specific size that will enable us to maximize the coercivity as we remain in the single domain limit.

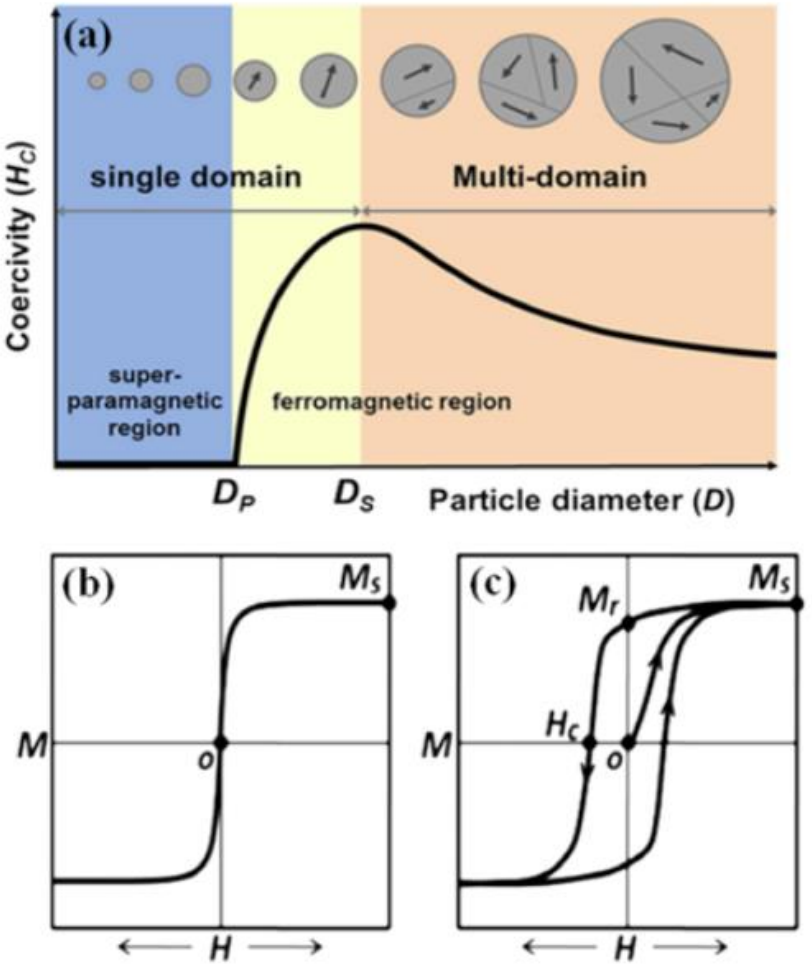

Figure 2.6. Scheme illustrating (a) size-dependent magnetic coercivity relationship of magnetic nanoparticles (49) and a typical hysteresis loop of (b) single-domain superparamagnetic nanoparticles and (c) single-domain ferromagnetic nanoparticles (50)

For a single domain nanoparticle, the magnetization is related to its anisotropy energy. The magnetic energy of a nanoparticle depends on the direction of its magnetization vector as shown in figure 2.6.

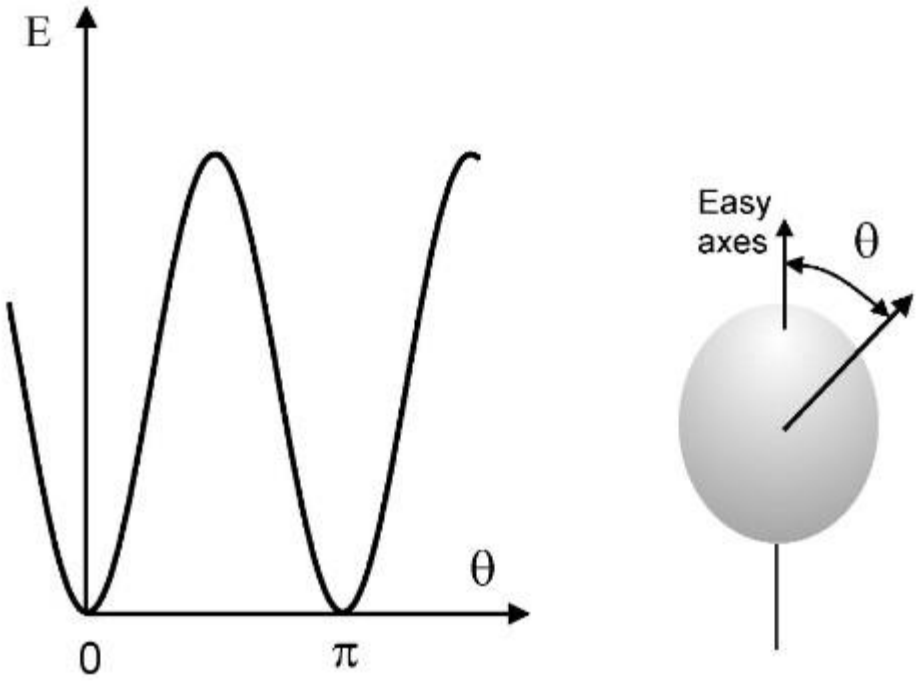

Figure 2.7. The relationship between the magnetic energy as a function of changing the angle between the magnetization vector and easy axis (30)

The direction with the minimum magnetic energy is called the anisotropy direction or easy axis and is dependent on the crystal structure of the particle. The magnetic energy increases with the increase of the angle between the magnetization vector and the easy axis. The amplitude of this curve is called the anisotropy energy.

The anisotropy energy is proportional to the volume of the particle given by (30):

$$E_a = K_a * V * sin^2(\theta)$$

Where E_a is the anisotropy energy, K_a is the anisotropy constant, V is the volume of the particle and θ is the angle between the magnetization and the easy axis.

The Neel relaxation time also depends on the anisotropy energy, as figure 2.7 shows the anisotropy energy gets its minimum value when θ = 0 or π. These two orientations that are antiparallel to each other have the lowest magnetic energy, so they are the stable states. Therefore, the magnetic moment in a single domain nanoparticle usually orients in these orientations that are separated by anisotropy energy barriers. At a finite temperature, there is a finite probability for the magnetization to jump over the energy barrier and reverse its direction. This process is called the Neel relaxation, and the mean time required for the jumps between different easy directions is the Neel relaxation time, τ_N and is given by:

$$\tau_N = \tau_0 \exp \frac{E_a}{kT}$$

Where E_a is the anisotropy energy, k is Boltzmann constant, T is the absolute temperature and τ_0 is a length of time in the range between 10^{-11} and 10^{-9} s.

According to the equation, τ_N increases when E_a increases; however, τ_0 decreases when E_a increases. For small anisotropy energy and high temperatures, E_a <<kT, the Neel relaxation time mainly depends on τ_0 which decreases as E_a increases. On the other hand, for large anisotropy energy and high temperatures, E_a >> kT, the Neel relaxation time mainly depends increases rapidly as E_a increases.

To sum up, the magnetic properties of nanoparticles rely heavily not only on the crystal structure but also on the size of the particles(51–53).

2.3. Optical Isolators

Optical isolators allow light to propagate in one direction, they are non-reciprocal devices and thus, must utilize a non-reciprocal phenomenon to function. The phenomenon used in optical isolators is Faraday rotation. For optical communication, several wavelengths are used in the infrared region typically around 850, 1300 and 1550 nm. These wavelengths are used because the attenuation of the transmission is much less at those wavelengths.

2.3.1. State of the art optical isolators

In this section, we will explain a few designs for optical isolators for both bulk isolators and integrated isolators.

2.3.1.1. Bulk Isolators

Optical isolators as previously mentioned only allow light to propagate in one, utilizing a non-reciprocal phenomenon which is Faraday rotation. Faraday rotation is a non-reciprocal rotation of the polarization of light, it is non-reciprocal in the idea that the rotation is not dependent on the direction of light propagation. If light propagates through a Faraday rotating medium, after a single pass the polarization is rotated by an angle θ, after a round-trip the polarization is rotated by an angle of 2θ.

An example is shown in Figure 2.8, using birefringent walk-off plates (BWP). At the BWP light is separated into the transverse magnetic (TM) and transverse electric (TE) polarizations. The TM polarization is vertical, while the TE polarization is horizontal. Figure 7.1 shows light entering the BWP, typically the TM light is transmitted straight through, while the TE light is transmitted away from the normal of the beam splitter. In the forward direction, light passes through the first beam splitter, then through the Faraday rotator and half-wave plate and finally a second beam splitter. The Faraday rotator provides a non-reciprocal 45° rotation and the half-wave

plate provides a reciprocal 45° rotation. This combined effect of the reciprocal and non-reciprocal effects transforms the TM light to TE and vice versa TE light to TM. At the second walk-off plate, the TE light is bent away from the normal while the TM passes straight through, both beams will then combine at a common output. However, in the reverse direction, the sequences of half-wave plate and Faraday rotator leave the TE and TM light unaltered. At the first walk-off plate, the two polarizations will exit at separate ports, thus the input is isolated.

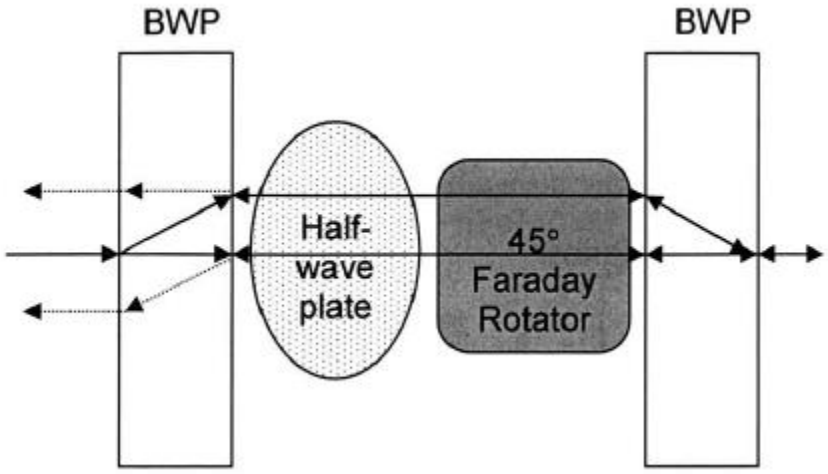

Figure 2.8. Bulk optical isolator example consisting of a half-wave plate, Faraday rotator, and BWP(2).

For optical communications an integrated form of the optical isolator is needed. As the optical networks continue to grow, growing more complex, greater integration of optical functions is needed to increase the capacity while reducing costs.

As Figure 2.9 shows, the isolator is the largest element in the laser package. The package consists of two polarizers, a Faraday rotator and an external magnet to bias the Faraday rotator. Reducing the size of laser packages as the one shown in Figure 2.9, will allow for several lasers to be integrated on a single chip.

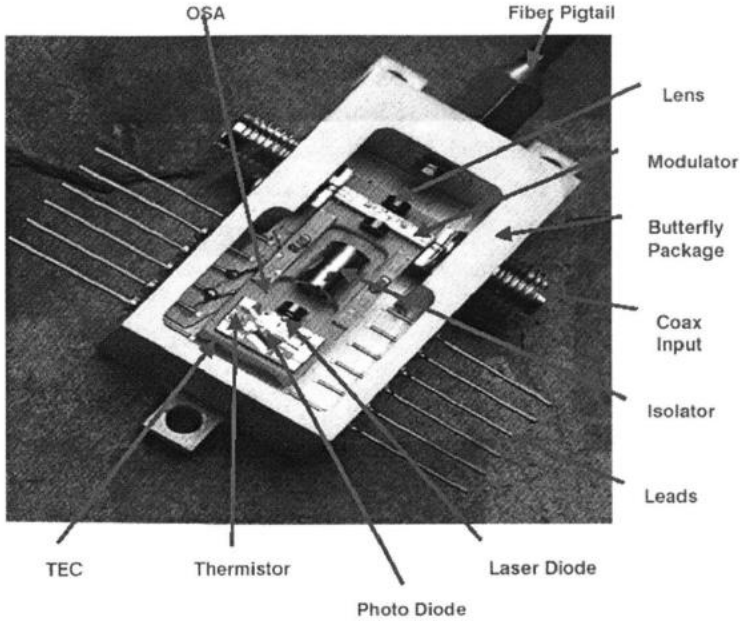

Figure 2.9. Optical isolator in a Laser package(2).

Moreover, integrated isolators are of importance for all-optical networks. The motivation for this type of networks is the need for higher network speeds. Currently, communication networks use electronics to process information contained in optical data packets to determine their destination. Optical-networks aim to do this in the optical domain using optical switches. Current research is being done using semiconductor optical amplifiers (SOA) for these types of switches.

Figure 2.10 shows an all-optical network. Two stages of optical SOQ switches are present in this network. For the best functionality, the stages should be buffered so that each individual stage's function is not corrupted by noise from other stages. The main sources of noise would be amplified spontaneous emission from the SOAs and back-reflection between stages. For this type of circuit, it would be practical that the isolators are in integrated form.

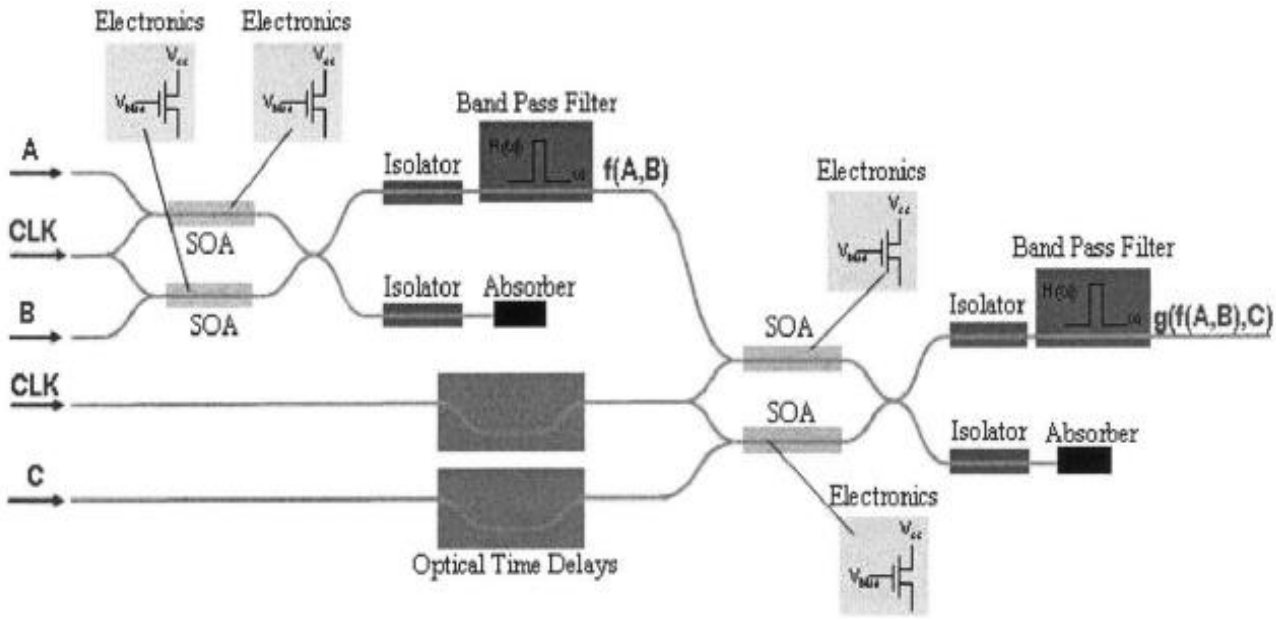

Figure 2.10. SOA switches(3).

2.3.1.2. Integrated Isolators

Three main approaches have been utilized to achieve integrated optical isolators. The first approach utilizes a magnetic field applied transverse to the direction of propagation of light which is labelled the non-reciprocal phase shift (NRPS), while the second approach utilizes a magnetic field parallel to the direction of propagation labelled as the non-reciprocal loss (NRL). The third approach is utilizing the Faraday rotation of magnetic particles to achieve isolation in waveguides, which is the approach used in this thesis.

2.3.1.2.1. Non-reciprocal phase shift (NRPS)

The magnetic field of NRPS is typically applied transverse to the direction of propagation of light as shown in Figure 2.11. The NRPS is a waveguide effect, occurring because of the coupling of transverse and longitudinal field components. Waveguide modes are divided into two types: TE and TM modes. The TE modes are typically dominated by an electric field in the y direction and negligible component in the x direction. While for TM modes, the y component has a negligible component with the x direction having a more dominant component.

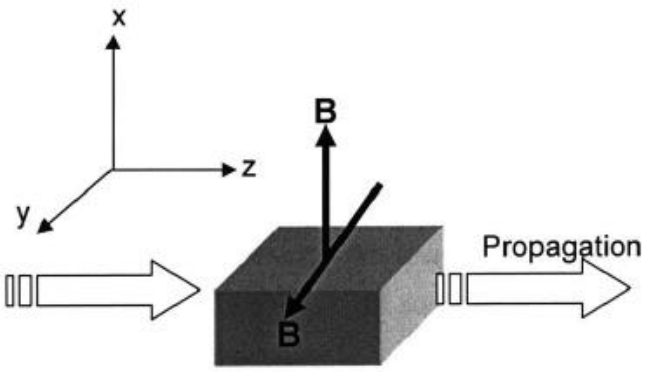

Figure 2.11. Configuration for NRPS(3).

To make an isolator using NRPS phenomenon, a Mach-Zehnder configuration is used. The NRPS waveguide is placed in one arm of the isolator and a reciprocal waveguide in the other. As light propagates in the forward direction, light in both arms will be in phase at the output and interfere constructively, traveling through the output port. However, in the reverse direction, the two arms will be 180° out of phase due to the NRPS. The light propagating in the reverse direction will interfere destructively and not be transmitted through the input port, thus isolation achieved. Isolators with 18 dB isolation have been achieved in magnetic garnets(54). The diagram of the isolator is shown in Figure 2.12. There exists two NRPS waveguides on each with opposite magnetization. Two electromagnets provided the external magnetic fields. The isolator is 8mm long, with NRPS waveguides which are 3.3 mm long. The waveguides are made from a bismuh-, lutetium-, and neodymium-iron garnet film $(Bi,Lu,Nd)_3(FeAl)_5O_{12}$.

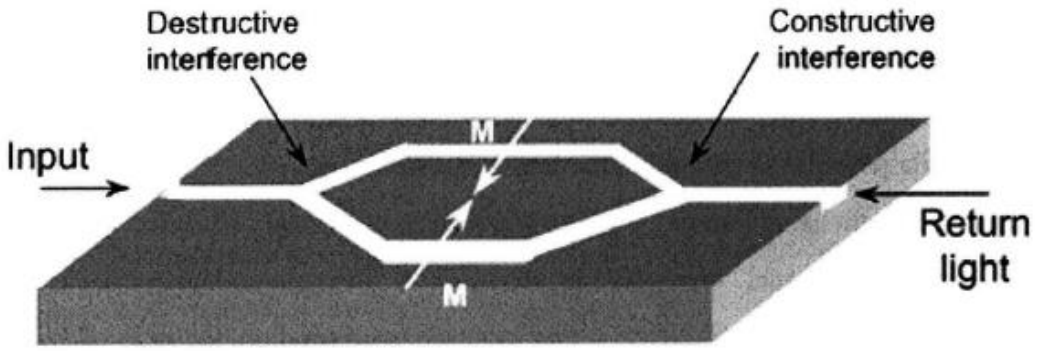

Figure 2.12. NRPS isolator using a Mach-Zehnder configuration(54).

2.3.1.2.2. Non-reciprocal loss (NRL)

NRL isolators are typically made by placing an absorbing magnetic layer on top of an SOA, as shown in Figure 2.13 (55). This isolator shows a theoretical isolation of 119 dB/cm for the TM mode. NRL isolators have been researched extensively and the best reported isolation was reported to be around 32 dB/cm (56). NRL isolators have several advantages over NRPS, first is that they do not need to be placed in a Mach-Zehnder configuration to function. Second, the maximum isolation is only limited by the device length which allows for incredibly high isolations to be achieved.

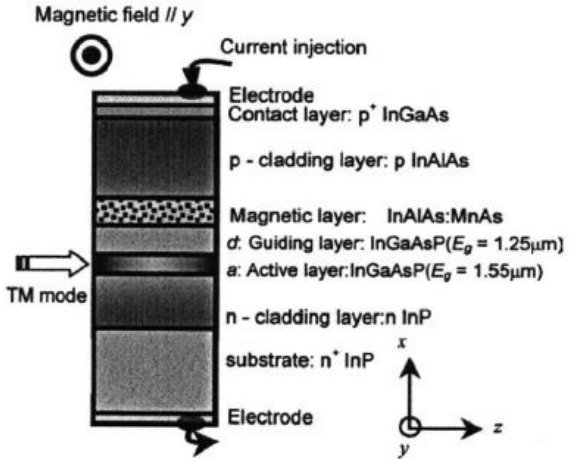

Figure 2.13. NRL isolator made using SOA and a magnetic absorbing layer (55)

However, NRL isolators have one particularly important disadvantage. The insertion loss for NRL isolators is typically very large. This is due to the fact that the optical modes penetrate into the absorbing magneto-optic layer.

2.3.1.2.3. Faraday Rotation for waveguides

Faraday rotation is utilized to make bulk optical isolators, however, for waveguide structures Faraday rotation is more difficult to utilize because of the strict phase-matching conditions. However, if the phase-matching conditions are achieved, the Faraday rotation can be utilized to make isolators of sizes which are an order of magnitude smaller than NRPS and NRL isolators.

For the purpose of this thesis, where there is light propagating inside the waveguides, light is described as an electromagnetic (EM) wave or field, that propagates in three dimensional space (57). An EM wave is composed of both an electrical component and a magnetic component that

travel combined through space (free space or transparent media). EM waves are characterized by wave, amplitude, phase, speed and polarization. Mathematically, EM field is specified by electric and magnetic field vectors, that are oscillating perpendicularly to each other and to the direction of propagation. The propagation of the EM field in medium can be fully described by Maxwell's equations, which take the following form(58):

$$\nabla \times \mathbf{E} = -\frac{\partial \mathbf{B}}{\partial t}$$
$$\nabla \times \mathbf{H} = \mathbf{J} + \frac{\partial \mathbf{D}}{\partial t}$$
$$\nabla \cdot \mathbf{D} = \rho$$
$$\nabla \cdot \mathbf{B} = 0$$

J is the electric current density and **ρ** is the total charge density. **E** and **B** are the electric and magnetic field vectors respectively, and **D** and **H** are the electric displacement and magnetic induction vectors respectively(59).

The speed of the EM waves is related to the angular frequency (ω), and EM wavelength (λ) through:

$$\omega = \frac{\lambda}{v}$$

Through this thesis, we can approximate that the EM waves are traveling in structures approximated by a "lossless" dielectric media. This helps us simplify Maxwell's equations by replacing **J = ρ = 0**, thus obtaining the following simplified form of Maxwell's equations(59,60):

$$\nabla \times \mathbf{E} = -\mu_0 \frac{\partial \mathbf{H}}{\partial t}$$
$$\nabla \times \mathbf{H} = \varepsilon \frac{\partial \mathbf{E}}{\partial t}$$
$$\nabla \cdot \mathbf{E} = 0$$
$$\nabla \cdot \mathbf{H} = 0$$

The first equation can be transformed into vectorial wave equations by applying the vectorial rotation operator (∇x), thus describing the electric and magnetic fields as follow:

$$\nabla^2 \mathbf{E} = \mu_0 \varepsilon \frac{\partial^2 \mathbf{E}}{\partial t^2}$$

$$\nabla^2 \mathbf{H} = \mu_0 \varepsilon \frac{\partial^2 \mathbf{H}}{\partial t^2}$$

These wave-equations of this form are known as homogenous wave equations(58,59). There exists an infinite number of solutions to the wave equation however, the simplest type is in the form of a traveling time harmonic plane wave. Traveling time harmonic plane waves are waves whose surfaces of constant phase with infinite planes that are perpendicular to the direction of propagation. EM waves consist of both magnetic field (**H**) and electric field (**E**) that oscillate perpendicularly to each other with respect to the direction of propagation (**k**).

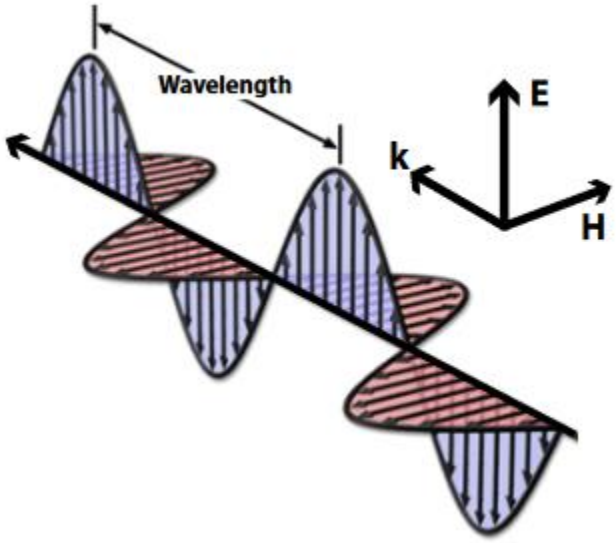

Figure 2.14 EM wave propagating in the direction of the wavevector perpendicular to both the electric and magnetic fields

Both the electric and magnetic field will have to be represented in the form of plane harmonic waves in the form(58,59):

$$\mathbf{E}(\mathbf{r},t) = \mathbf{E_0} e^{-i(\mathbf{k}\cdot\mathbf{r}-\omega t+\phi_0)}$$

$$\mathbf{H}(\mathbf{r},t) = \mathbf{H_0} e^{-i(\mathbf{k}\cdot\mathbf{r}-\omega t+\phi_0)}$$

$\mathbf{H_0}$ and $\mathbf{E_0}$ represent the field-intensity vector (amplitude and polarization) of the magnetic and electric components respectively. **r** is the position vector, **k** is the wave-vector and $\boldsymbol{\phi_0}$ is an arbitrary phase angle. $\omega = 2\pi f$ is the angular frequency of the wave.

EM waves propagate through waveguides by total internal reflection, as the waves propagate through an evanescent wave is generated when the conditions are met. Figure 2.15 shows a representation of a plane wave reflection at an interface.

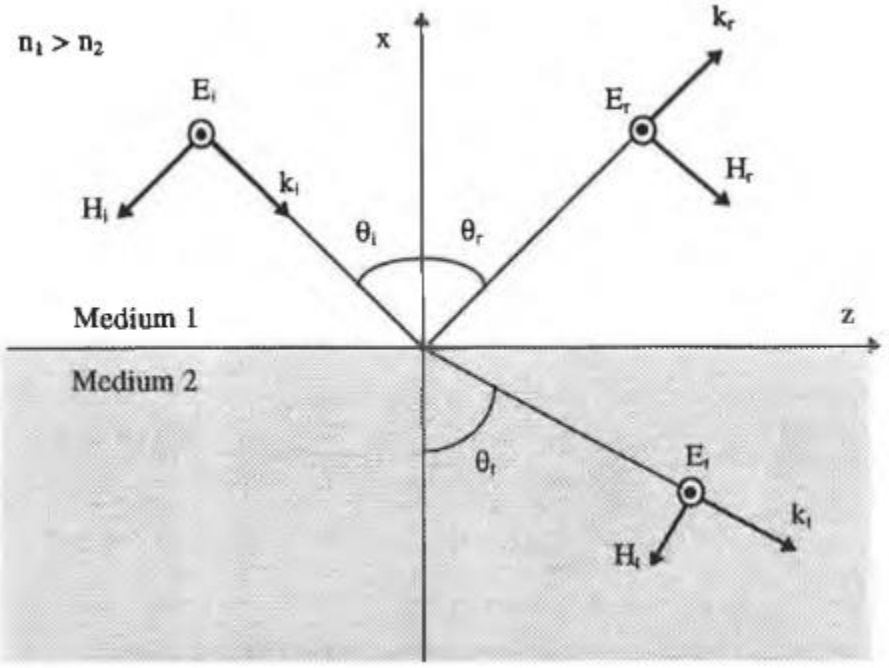

Figure 2.15 Plane wave reflection from a dielectric interface represented in terms of E, H and k vectors(58).

To obtain a mathematical description of what occurs at the interface, it is convenient to take the simplest case where a non-magnetic dielectric media is present. The incident (i), reflected (r) and transmitted (t) plane waves are then represented by(58,59):

$$\mathbf{E}_i = \mathbf{A}_i \cdot e^{-j(\mathbf{k}_i \cdot \mathbf{r} - \omega t)}$$

$$\mathbf{E}_r = \mathbf{A}_r \cdot e^{-j(\mathbf{k}_r \cdot \mathbf{r} - \omega t)}$$

$$\mathbf{E}_t = \mathbf{A}_t \cdot e^{-j(\mathbf{k}_t \cdot \mathbf{r} - \omega t)}$$

Where A is the electric field amplitude and t is the time. It can be shown using Maxwell's equations that the tangential components of **E** and **H** fields must be continuous across the boundary between the two media. Thus, the phase variation along the interface must be the same for the incident, reflected and transmitted fields.

$$K_i.r = K_r.r = K_t.r$$

This concept of evanescent waves yield the optical modes inside the waveguides similar to the figure below(61). This aids us in understanding the polarization of light can be changed by the addition of thin films or nanoparticles on top of the waveguides and not necessarily inside the waveguides. As these films or nanoparticles will be capable of transforming the transverse electric waves entering the waveguide to transverse magnetic waves causing optical isolation(61).

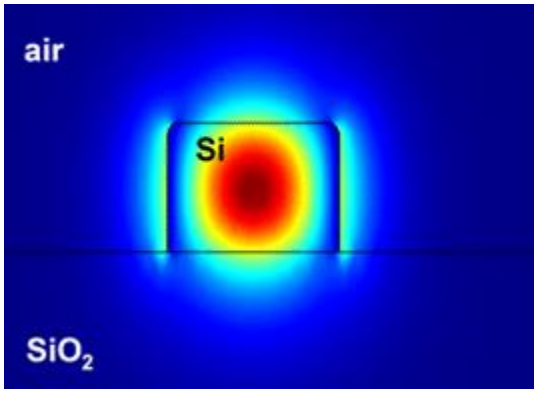

Figure 2.16. The distribution of TE mode optical field inside Si waveguide(61,62).

Waveguide Faraday rotation has been demonstrated in magnetic garnets (63). Faraday rotation were shown in dilute magnetic semiconductor (CdMnTe/GaAs) waveguides(62). There have also been proposals for InGaAs/InP waveguide Faraday rotators with a magnetic garnet layer(64). However, the biggest challenge with waveguide Faraday rotation is that the transverse electric (TE) and transverse magnetic (TM) modes must be properly phase matched or else the Faraday rotation is suppressed. Faraday rotation can be stated as the coupling of the TE and TM modes. If phase mismatch (birefringence) are present, then the total power transfer between the modes is not possible. Thus, a suppression in Faraday rotation is seen. Figure 2.17 shows the Faraday rotation for a magnetic garnet, a high birefringence waveguide, a low birefringence waveguide. As the length of the Faraday rotator is increased, the high birefringence waveguide's Faraday rotation oscillates, while the bulk sample and low birefringence waveguides show an increase in their Faraday rotation.

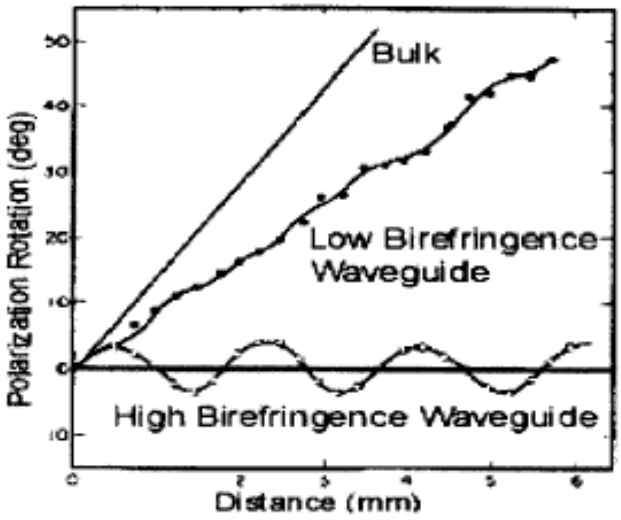

Figure 2.17. Faraday rotation vs length for three different magnetic garnet samples: a bulk sample, a high birefringence waveguide, and a low birefringence waveguide (98)

Isolators have been achieved with waveguide Faraday rotators (65). In this thesis, we are proposing to utilize the best magnetic nanoparticles synthesized in chapter 4 as Faraday rotators to attempt optical isolation on silicon waveguides.

2.3.2. Nanoparticle Faraday rotation

Application of nanomaterials have been shown to yield Faraday response enhancing the optical properties over that of the bulk material (66). This has been proven useful for telecommunication specifically for materials that are sub 20 nm in size which can produce less scattering (67).

In the last 20 years, ongoing research has been able to show that several nanoparticles' material have shown enhanced Faraday rotation, including Fe_2O_3 nanoparticles (6). Several authors were able to experimentally and theoretically calculate the required size of the nanoparticles while showing an enhancement in Faraday rotation (39).

Dani et al.(6) were able to calculate the theoretical Faraday rotation expected, from Fe_2O_3 and gold coated Fe_2O_3 nanoparticles, where the calculations were made over the ultraviolet region between 350 nm < lambda <700 nm. The Drude model for the electron response can be used to estimate the absorption and Faraday rotation effects of the Fe_2O_3. A resonance in the absorption will correspond to a similar resonance effect in the Faraday rotation. First, an accurate description of the dielectric functions $\varepsilon(\omega)$, based on experimental measurements of absorption in solutions of nanoparticles was found. Once $\varepsilon(\omega)$ is known for the nanoparticles, the resulting Faraday rotation can be calculated as described below.

The frequency-dependent relative dielectric permittivity of a medium, due to bound electrons at a single resonance ω_0 combined with free electrons of plasma frequency ω_p, is taken as(60,68):

$$\varepsilon = 1 - \frac{g_0^2}{\omega^2 - \omega_0^2 + i\gamma_0\omega - \nu\omega\omega_B} - \frac{\omega_p^2}{\omega^2 + i\gamma_p\omega - \nu\omega\omega_B}$$

For the bound electrons, ω_0 is the binding frequency, g_0 is the oscillator strength, and γ_0 is the damping frequency. The last term in the equation above represents the free electrons, with plasma frequency ω_p and damping frequency γ_p. The applied magnetic field (along z) responsible for the Faraday rotation enters into both terms, in the cyclotron frequency, $\omega_B = eB_z/m^*$. The helicity is $\nu = +1/-1$ for left/right circular polarization. That term, due to the Lorentz force, leads to Faraday rotation.

Describing the maghemite core is more complex, as the γ-Fe_2O_3 has several absorption resonances. There exists one strong absorption resonance in the UV region responsible for Faraday rotation. The results are for iron oxide nanoparticles suspended in water (host medium). For a volume fraction f of spherical particles of dielectric constant ε in water (the host medium, with ε_a=1.777), the absorption is $\alpha = 2\frac{\omega}{c}\mathrm{Im}\{\sqrt{\varepsilon_{\mathrm{eff}}}\}$, where $\varepsilon_{\mathrm{eff}}$ results from the Maxwell Garnett effective medium theory (69) (MG equation):

$$\frac{\varepsilon_{\mathrm{eff}} - \varepsilon_a}{\varepsilon_{\mathrm{eff}} + 2\varepsilon_a} = f\frac{\varepsilon - \varepsilon_a}{\varepsilon + 2\varepsilon_a}$$

Dani et al's calculations for maghemite coated with a gold shell shows that it can theoretically yield up to 10 rad/Tm for nanoparticles with an average radius of 4.85 nm in the UV region between 350 < lambda < 700 nm. They were only able to experimentally observe Faraday Rotation for gold shell coated iron oxide core nanoparticles where they found 3 rad/Tm to 10 rad/Tm for a gold shell of 5nm coated on a 10nm Fe_2O_3 core measured at a wavelength of 632 nm.

2.4. Reverse micelles for nanoparticles synthesis

Different methods have been deployed to synthesize nanoparticles with a wide range of diameters. The simplest approach is ball milling of the corresponding bulk materials. This approach will yield a broad size distribution, which as a result will hamper the study of size-dependent properties (70). A better approach is inert-gas condensation where the nanoparticles are formed by sputtering from a target which will then agglomerate into clusters

in an environment where there is a continuous gas flow before landing on a support (71,72). This approach is very advantageous mainly in the selection of specific sizes required during flight(73,74), however, the nanoparticles are deposited randomly on the substrate. This affects the studying of the properties of the nanoparticles that are of interest and yields low coverage of the nanoparticles in most cases. This could be solved partially by landing the nanoparticles on a polymer matrix (75), or by using a biotemplate(76).

The impressive growth in organometallic chemistry has revolutionized the field of small particles for more than a decade (77,78). Surfactant-mediated growth of nanoparticles with narrow size distributions from metal precursors in solution opened the field of self-assembly, which allows the formation of largescale ordered nanoparticles (79–81). Over the years this method has been optimized and enhanced to synthesize nanoparticles with tunable diameters, small size distributions with small nm interparticle spacings and additionally, the flexibility to produce a monatomic layer of nanoparticles as well as bimetallic nanoparticles (82,83). One of the recent advancements is employing diblock copolymers self-assembly templates offering rigid space confinement (84). The diblock copolymers consist of two chemically different blocks with one non-polar (hydrophobic) and another polar (hydrophilic). With selective non-polar solvents, the diblock copolymers can form reverse micelles with the corona of non-polar blocks surrounding the core of polar blocks (85). A variety of diblock copolymers exist, the different diblock copolymers are adopted to produce different nanoparticles which include but are not limited to metals, metal oxides and metal alloys (86).

Various types of diblock copolymer exist (87–89), the polystyrene-b-poly(vinylpyridine) (PS-b-PVP) families including PS-b-P2VP and PS-b-P4VP are frequently used to synthesize nanoparticles. PS(x)-bP2VP(y), where x and y denoted the number of monomers per block, and thus, determine the length of each block. By nature, the PS- block is hydrophobic and the P2VP-block is hydrophilic, this enables us to produce reverse spherical micelles in apolar solvents(90,91).

In the diblock copolymer reverse micelles procedure, the diblock copolymer is dissolved in xylene, to form the reverse micelles with non-polar PS corona and polar PV core. The proper precursor metal salt is added and infiltrated inside the polar core. Then, the loaded micellular solution is coated on a silicon substrate by spin-coating. In the next step, nanoparticles are formed on the substrates by exposure to oxygen plasma which will etch the polymer and simultaneously form metal-oxide nanoparticles. The figure below shows and summarizes the exact procedure.

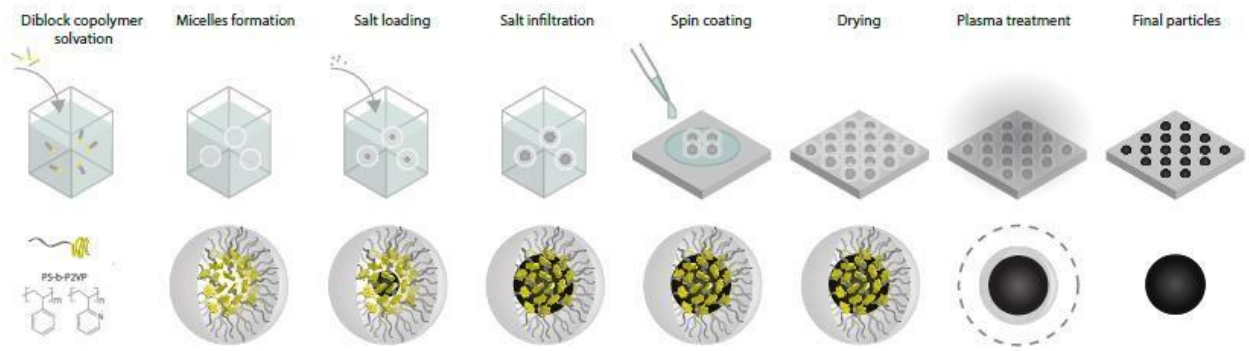

Figure 2.18. Preparation of nanoparticles using the diblock copolymer reverse micelles(92).

The diblock copolymer reverse micelles synthesis procedure has significant advantages:

1) The nanoparticles synthesized are homogenous in shape. All the nanoparticles synthesized are spherical in shape, which is not the case for most of the other procedures.
2) Narrow size distribution throughout the sample. The distribution between the nanoparticles is narrow and tunable offering excellent flexibility.
3) Production of spatially ordered arrays of nanoparticles. Diblock copolymer reverse micelles produce a spatially ordered arrays of nanoparticles in the 2-D periodic lattice.

2.4.1. PS-b-P2VP reverse micelles formation and parameters

PS-b-P2VP reverse micelles are typically formed in a selective solvent for the non-polar polystyrene (PS) blocks when the concentration of the PS-b-P2VP is above the critical micelles concentration (CMC). The CMC is the concentration of a surfactant in a bulk phase above which micelles start forming(93). Oxylene is typically used as a solvent forming the reverse micelles (90,91). The CMC for the PS-b-P2VP was found to be around 0.1mg/ml (94). As the micelles form, the hydrophobic PS blocks align towards the solvent-polymer interfaces to form the corona of reverse micelles, while the hydrophilic P2VP block is concentrated towards the inside forming the core of the reverse micelles. Figure 2.19 shows the schematic for reverse micelles formation.

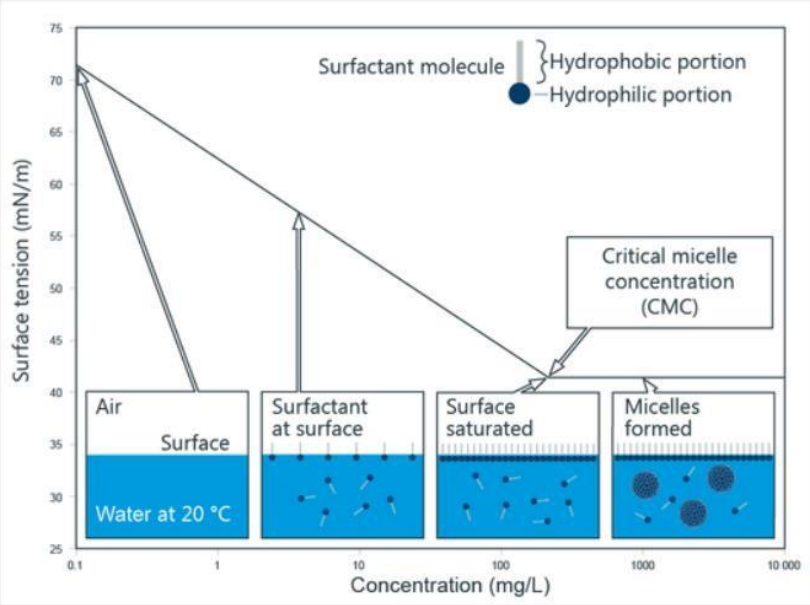

Figure 2.19. Schematic for reverse micelles formation (62).

Moreover, the size of the micelles is unchanged as the concentration is varied between 1 mg/ml and 5 mg/ml (65). The size of the micelles is corelated to the aggregation number, which is the total number of diblock copolymer molecules in single micelles. This can be altered with the block length of PS or P2VP (64), thus obtaining different sizes of micelles by varying the molecular weight in PS or P2VP block of PS-b-P2VP.

2.4.2. Precursor salts

An iron salt $FeCl_3$ was found to be a suitable precursor to be a suitable salt to load in the PS-b-P2VP reverse micelles (25,87,95). Very similar to the procedure explained in figure 2.18, oxygen plasma is deployed to remove the carbon-based micelles and oxidizing the $FeCl_3$, together by annealing of the sample to increase the crystallinity of the nanoparticles and produce iron oxide nanoparticles (66).

$$4FeCl_3 + 3O_2\ (Plasma\ etching) \rightarrow 2Fe_2O_3 + 3Cl_2$$

Tin oxide nanoparticles have been widely interesting and have shown some ferromagnetic properties(34,37,44), this is explained by some authors as a result of the presence of oxygen vacancies in the SnO_2 nanosystems (37,44).

For tin oxide synthesis, $SnCl_2$ was loaded in the PS-b-P2VP reverse micelles. The reverse micellular route is applicable for the synthesis of tin oxide nanoparticles with an additional step of adding ethanol(89,96)

$$SnCl_2.2H_2O + C_2H_5OH\ (ethanol) \rightarrow Sn(OH)_2 + C_2H_5Cl + H_2O$$

After loading ethanol into the loaded micelles solution, the resulted solution is plasma etched to remove the organic micellar layers and expose the corresponding tin oxide nanoparticles.

$$Sn(OH)_2 + O_2\ (Plasma\ etching) \rightarrow 2SnO_2 + 2H_2O$$

2.5. Different characterization techniques for iron oxide nanoparticles

The properties of the nanoparticles are tested in a variety of ways using different characterization techniques, these techniques are helpful to identify the crystal structure of the particles, the size and distribution of the particles and their magnetic properties.

Raman spectroscopy is one of the vibrational spectroscopic techniques which helps provide information of molecular vibrations and crystal structures. It is an inelastic process, which aids in providing detailed information about the material based on vibrational modes of the phonon. When light is scattered from a molecule or a crystal, most phonons are scattered elastically with the same frequency and energy as the incident photons. However, a small fraction of light is scattered inelastically with a frequency lower than the incident photons. The process leading to this inelastic scatter is dubbed the Raman effect. If the scattering is elastic, the process is called Rayleigh scattering. If it's not elastic, the process is called Raman scattering (97).

Raman effects will arise when a photon is incident on a molecule and interacts with the electric dipole of the molecule. The scattering will be described as an excitation to a virtual lower state in energy than a real electronic transition with nearly coincident de-excitation and a change in vibrational energy. The vibrational state of the scattering is shown in figure 2.20.

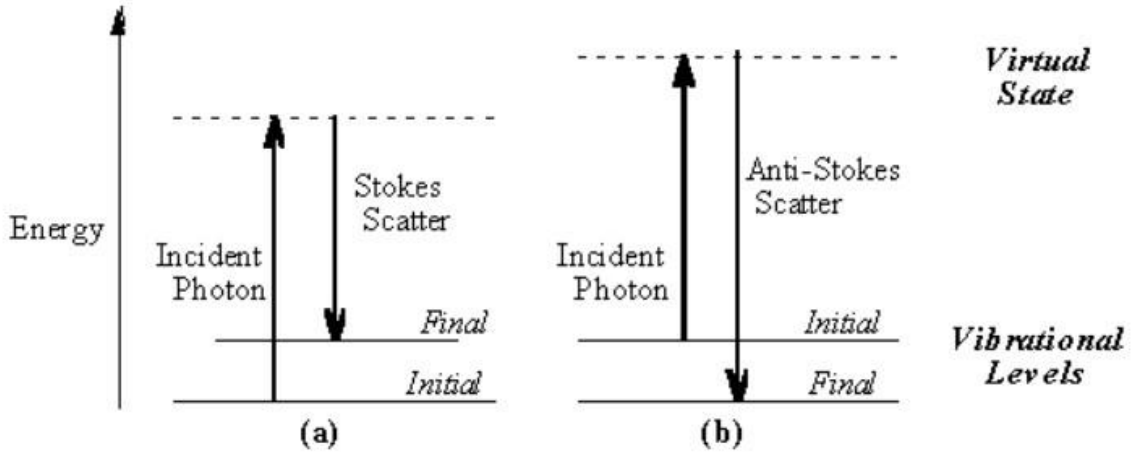

Figure 2.20. Energy level diagram for Raman scattering; Stokes scattering (a), anti-Stokes scattering (b)

To investigate the properties of FeCl3 (98,99), $SnCl_2$ (100) and PS-b-P2VP (101) Raman spectroscopy has been a great choice to investigate the evolution of the nanoparticles from the early stages of synthesis using PS-b-P2VP, $FeCl_3$ and $SnCl_2$ which will be examined in chapter 4 mainly.

Moreover, we need a technique to investigate the individual nanoparticles in terms of size, dispersion, interparticle distance and nanomechanical properties. Atomic force microscopy (AFM) was used to measure the morphology of the nanoparticles on a flat surface. AFM is a type of scanning probe microscopy, which enables us to measure the height with great accuracy on the order of fractions of nanometers. Traditionally, most AFMs use a laser beam deflection system where the laser is reflected off the back of the reflective AFM lever. Moreover, Quantitative Nanoscale Mechanical Characterization (QNM) was used to distinguish between the nanomechanical properties including modulus, adhesion, dissipation and deformation.

Finally, to measure the magnetic properties of the nanoparticles, superconducting quantum interference device magnetometer (SQUID) is used for applications with small amount of material such as thin monolayer of nanoparticles (102,103). The SQUID is a device which is used to transduce magnetic flux into voltage. The SQUID operates on the Josephson Effect and magnetic flux quantization phenomena which enable us to recover very sensitive magnetic flux data by transducing the magnetic flux to voltage. The SQUID is very sensitive due to its low thermal noise characteristics and high magnetic flux sensitivity which enables us to test our monolayer of nanoparticles (104).

Chapter 3

Experimental

3.1. Materials

Polystyrene-block-poly (2-vinyl pyridine) (PS-b-P2VP, M_n: 75000-b-66500) often referred to as P4824, and (PS-b-P2VP, M_n: 28000-b-36000) often referred to as P9861 were used during my thesis. The polymers were purchased from Polymer source Inc. as described below to be used in the reverse micelles approach. The Iron (III) chloride ($FeCl_3$, sublimed grade, ≥ 99.9%), o-xylene (reagent grade, ≥ 98.0%) and stannous chloride ($SnCl_2$. $2H_2O$) were purchased from Sigma-Aldrich. Ethanol (95% vol) was also used during the synthesis of SnO_2 nanoparticles and was purchased from Commercial Alcohols.

3.2. Cleaning

The silicon substrates and vials were immersed in a clean beaker with acetone for 15 minutes in an ultrasonic (ultrasonic cleaner, VGT-1620QTD) bath treatment followed by another 15 minutes in 2propanol in an ultrasonic bath treatment. A N_2 gun was used to dry the substrates and the vials after solvents cleaning.

3.3. Synthesis of the nanoparticles

3.3.1. PS-b-P2VP fritting

Prior to dissolving the diblock copolymer in o-xylene, the PS-b-P2VP polymers were fritted to remove undesirable oxidation. 10 mL of Tetrahydrofuran (THF) was added into a vial containing the polymer to be fritted, the vial is sonicated for 30 minutes to ensure that the polymer is dissolved in THF. The solution produced is fritted using a glass fiber and precipitated into a 200 mL of hexane stirred at 500rpm. Using a fine pore size filter funnel with the aid of a vacuum pump we are able to collect the precipitates; the precipitates are left to dry overnight under ambient conditions before collecting them for further usage.

3.3.2. Reverse micelles formation and salt loading

Reverse micelles of PS-b-P2VP are formed when the fritted copolymer (P9861 or P4824) is dissolved in xylene to yield solutions above the critical micelle concentration (65), typically between 3.00-3.75mg/ml.
The solutions are kept under magnetic stirring to facilitate the reverse micelles formation. The non-polar PS are highly soluble in o-xylene, this enables the PS blocks to align towards the solvent-polymer interfaces to form the corona of reverse micelles, while the P2VP block is concentrated towards the inside forming the core of the micelles. After 24 hours of magnetic stirring, salt loading inside the glove box for an oxygen free environment as the salts are very sensitive to oxygen.

3.3.2.1. Iron chloride salt loading

Typically, after 24h stirring, the iron precursor $FeCl_3$ is added to the reverse micelles solution with various loading ratios (the ratio between the amount of Fe^{3+} and the total amount of 2-vinyl pyridine(2VP) units of the PS-b-P2VP (unit in mole)).

The standard loading ratio for $FeCl_3$ is 0.2. The ratio between Fe^{3+} and 2VP is used to calculate the amount of $FeCl_3$ to add:

$$\frac{n(\mathrm{Fe3+})}{n(2VP)} = 0.2$$

This yields an amount of 2.35 mg of $FeCl_3$ to be loaded. This calculation was done for P4824, it is slightly different for P9861 yielding 2.67 mg of $FeCl_3$.

The solutions are kept under further magnetic stirring for at least 24 hours to ensure adequate precursor loading.

3.3.2.2. Tin chloride salt loading

For tin chloride loading, the same procedure is applied as iron chloride loading with an additional ethanol step(96). After the fritted polymer of P4824 or P9861 is spun for at least 24 hours, the tin precursor $SnCl_2$ is added to the reverse micelles solution with various loading ratios (the ratio between the amount of Sn^{2+} and the amount of 2VP).

The standard loading ratio used in the thesis was 2.0. The ratio between Sn^{2+} and 2VP is used to calculate the amount of $SnCl_2$:

$$\frac{n(\mathrm{Sn2+})}{n(2VP)} = 2.0$$

This yields an amount of 16.9 mg of $SnCl_2$ to be loaded into the micelles solution. For $SnCl_2$ only P4824 polymer was used, the amount calculated above is for P4824.

The solution is kept under magnetic stirring for at least 48 hours to ensure adequate precursor loading. Then, an additional reagent is used to produce the SnO_2 nanoparticles. A small amount of Ethanol is decanted into a clean beaker, then using a pipette 0.300 mL of ethanol is poured into the Sn^{2+} loaded reverse micelles solution. The vial is covered tightly with parafilm and left to spin for at least 48 hours.

3.3.3. Substrate coating

The substrates used were Silicon for AFM and SQUID, and KBr for Raman purposes. The silicon substrates and vials are cleaned as described in 3.2. After adequate magnetic stirring of the reverse micelles solution, the reverse micelles have to be coated on the substrates. For spin coating, typically 4 µL is dynamically spin coated on the silicon substrates for 45 seconds at spinning rate of 2000 rpm. The spin coater used is Laurell Technologies Spin coater (WS650MZ-23NPP) and is used outside the glovebox. Moreover, for Raman spectroscopy the samples used are KBr samples. The samples are cleaved and cleaned using a N_2 gun. The coating of the KBr samples is different, the coating technique used is drop casting. 4 µL of the micelles solution is deposited in the center of the stationary KBr sample and left to dry. Typically for most of the KBr samples, three drop casts are required for adequate Raman response. The different materials used will be further explained in chapter 4.

3.3.4. Oxygen plasma treatment

The coated samples were plasma etched in an oxygen environment to remove the polymeric micelles and leave the iron oxide and tin oxide nanoparticles on the substrates. The plasma treatment was carried out in a Harrick Plasma cleaner (PDC-001-HP). The etching conditions were set as 29.6W power (medium) with 30 sccm O_2 gas flow for 25 minutes, which corresponds to about 950 mTorr in the plasma chamber.

3.3.5. Annealing

After oxygen plasma treatment, the silicon samples coated with the nanoparticles on are annealed in a Lindberg tube furnace where the coated substrates were kept in an alumina boat pushed into the middle of the furnace. The tube has glass caps on both ends, this enables us to have a N_2 flow. Different annealing conditions were deployed typically changing the annealing times. The full annealing conditions for all the samples are explained in chapter 4.

3.4. Characterization techniques

3.4.1. Raman Spectroscopy

Raman spectroscopy was performed by a Renishaw inVia spectrometer at 514nm laser excitation on drop casted (2 µL twice) samples on freshly cleaved KBr substrates. The laser power was set to 10mW and an objective of 20x and 1800 l per mm grating was used. To generate adequate signals for the spectra acquisition, the laser was focused at regions with visible residue ("coffee stain" area as the drop casted sample solution) where more materials were aggregated. The baseline of the spectra was created and then subtracted to highlight the peaks of interest. In addition, the spectra were smoothed by Savitzky-Golay function in Origin. The smooth spectra were normalized to 0-1 in the region from 150 cm^1 to 900 cm^{-1}. The processed spectrum features from 150 cm^{-1} to 900 cm^{-1}. were deconvoluted using Lorentzian line shape profiles to highlight the iron oxide characteristic peaks.

3.4.2. Atomic Force Microscopy (AFM)

The AFM substrates used were all silicon, the silicon wafers had a thickness of 500 µm, and <100) orientation. The AFM images were collected by an Asylum MFP-3D instrument (Oxford Instruments Asylum Research Inc.) in the alternating current mode in room temperature. AFM probes (Oxford Instruments Asylum Research Inc.) with a spring constant of 26 N/m and resonant frequency of 300 kHz were applied for the topography scans.

WSxM was used to process the AFM images (105). AFM images were taken on a scale of 1 µm x 1 µm and at a scanning rate of 0.5 Hz. The height of the nanoparticles was determined by taking a line profile through 100 nanoparticles and taking the average.

3.4.3. Superconducting quantum interference device magnetometer (SQUID)

The magnetic properties of the nanoparticles were measured by liquid cooled SQUID. The samples were created by cutting the 275µm thick Si substrates into a 40 mm by 5 mm stripes to accommodate the sample holder in the SQUID magnetometer. The center area of the Si substrate (5mm by 5mm) is the only area that was covered, and the loaded micelles solution is spin-coated at 2000 rpm for 45 seconds. The center area as mentioned is left uncovered, however the remaining of the Si substrate is covered by a small aluminum foil that is wide enough to cover the width of the substrate on both sides of the center of the substrate with aluminum tape on top of the foil to ensure that the loaded micelles solution does not slip to the sides. All SQUID samples were treated to 25 minutes with oxygen plasma before annealing. The measurements of the samples were performed at 300K with an applied magnetic field between -2000 Oe and 2000 Oe. Data points were collected by each 100 Oe increment between -5000 Oe and 5000 Oe, and by 100 Oe increments for the rest of the data set.

3.4.4. Quantitative Nanoscale Mechanical Characterization (QNM)

(Measurement & analysis done by Greg Hanta)

QNM was done using a Bruker Bioscope Catalyst with an RTESPA probe. The probe was selected to match the range of elastic modulus we were investigating based on recommendations by Bruker. For each round of measurements, the probe was calibrated using a relative method of calibration, using a sample of known modulus. The calibration first involves the calculation of the deflection sensitivity by ramping the probe into a clean sapphire substrate provided by Bruker. A minimum of three ramps were done and the average deflection sensitivity was used. The probe is then withdrawn from the substrate and a thermal tune is preformed to calculate the spring constant. Lastly, a polystyrene sample of known modulus provided by Bruker is loaded and imaged. The tip radius is adjusted until the measured modulus agrees with the known modulus. AFM images were taken on a scale of 1 µm x 1 µm and at a scanning rate of 0.5 Hz. The elastic modulus was determined by taking a line profile through 100 micelles by matching the coordinates in the topography channel to the elastic modulus channel. The elastic modulus for each micelle was determined by taking the average of the center points of the line profile. The number of points averaged to determine the modulus varied due to a range in the size of micelles measured. However, typically 10 points were taken. The modulus measurements for each micelle were fit using a Gaussian approximation to calculate the average modulus value and error for each treatment.

3.4.5. Scanning Electron Microscopy (SEM)

The substrates for SEM characterization were P-doped silicon wafers with thickness of 380µm, orientation of <100> and resistivity: 0.001-0.005 ohm-cm. These wafers are conductive enough to allow the direct SEM imaging of nanoparticles without coating. The nanoparticles coated substrates were mounted by carbon tape and nickel paste on 25.4mm standard Al stubs. The SEM characterizations were conducted in FEI Versa 3D SEM with a Schottky thermal field emitter electron gun. The accelerating voltage and probe current were normally adjusted to 5kV and 12pA to minimize the charging effect, which still maintained good signal-to-noise ratio for high quality imaging.

Chapter 4

Tracking of the Iron Oxide nanoparticles using Raman Spectroscopy[1]

4.1. Experimental

To use the iron oxide nanoparticles as optical isolators on silicon waveguides, we must make sure that the nanoparticles that are synthesized are in γ-Fe_2O_3 phase. The γ-Fe_2O_3 has been proven to be a good optical isolator as in the work of D. Hutchings et al.(106). We use Raman spectroscopy to be able to identify the best PS-b-P2VP polymer to use along with the optimum annealing conditions. In this chapter, the $FeCl_3$ loaded micelles and iron oxide nanoparticles were synthesized following the procedures in chapter 3. Two loading ratios were used, 0.2 and 1.5. The PS-b-P2VP used here were both P4824 (PS-b-P2VP, M_n: 75000-b-66500) and P9861 (PS-b-P2VP, M_n: 28000-b-36000).

The samples fabricated for the Raman characterization were drop-cast (4 µL for 3 times) on freshly cleaved KBr substrates. The solution used was $FeCl_3$ loaded in a P4824 or P9861 solution using o-xylene as a solvent. Following the synthesis processes in chapter 3, the KBr sample was oxygen plasma etched for 25 minutes before the annealing step. The same substrate was annealed at different conditions to investigate the phase transformation of the iron oxide nanoparticles. The Raman spectra for different samples annealed at different conditions using different polymers were collected. It is important to note that in order to get sufficient Raman signal, the laser was focused on regions with high concentration of materials, often referred to as the "coffee stain" which was visible as the sample solution dried off.

Scanning electron microscope (SEM) measurements were performed with a FEI VERSA 3D. SEM images were obtained using an accelerating voltage of 5kV and a probe current of 12pA. Atomic force microscopy (AFM) images were collected using an Asylum MFP-3D instrument (Oxford Instruments Asylum Research) in the alternating current (AC) mode under ambient environment. AFM probes (Oxford Instruments Asylum Research) with spring constant of

[1] This chapter is a modified version of "Multi-phase crystallization from manipulation of reverse micelle deposition: single crystalline Fe_2O_3 nanoparticles with tunable crystal structure" A. Ibrahim, R. Arbi, K. Liang, G. Hanta, L. S. Hui, A. Turak, submitted to Particle and Particle Characterization (2019)

26N/m and resonant frequency at 300kHz was engaged in tapping mode for topography scan. WSxM 5.0 was used for AFM image processing.(107)

To perform analysis of the micelle or nanoparticle sizes, SEM or AFM images were first imported into ImageJ.(108) To determine the sizes and locations of the micelles/particles, depending on the quality of the image, the images were either binarized, with ImageJ used directly to calculate the location and radius of each particle, or if the noise level of the image is too high, the size was found manually, by drawing an ellipse around the object. The major and minor radius measurements from either approach are used to find the approximate radius and area of the micelle. This was converted into an effective radius of a circular micelle for each particle. In general, a hundred measurements on different particles within a 2μm x 2μm area were sampled to determine the average radius and error from a histogram of the radii distribution.

Quantitative nanomechanical mapping (QNM) AFM was performed using a Bruker Bioscope Catalyst with an RTESPA probe. To confirm the mechanical properties of the micelles, hardness and Young's modulus maps were generated using the QNM AFM mode provided by the Bruker Nanoscope software. AFM images were analyzed in post using WSxM(107) (76). The elastic modulus was determined by taking a line profile through 100 micelles by matching the coordinates in the topography channel to the elastic modulus channel. The elastic modulus for each micelle was determined by taking the average of value at the center points of the line profile, correlated to the centre of the micelle in the topography channel. The number of points averaged to determine the modulus varied due to a range in the size of micelles measured. However, typically 10 points were taken. The modulus measurements for each micelle were fit using a Gaussian approximation to calculate the average modulus value and error for each treatment.

All SEM, AFM and QNM samples was prepared by dynamically spin-coating 4ul of solution on to a 1x1 cm^2 Si substrate inside a glovebox at 2000rpm for 45s (Specialty Coating Inc. G3P spin coater).

To determine the inner core diameter of the micelles, a thin layer of micelles was deposited to the porous carbon thin film TEM grids by using dip-coating, which allowed direct TEM/STEM characterization of the individual micelles. In order to selectively stain the P2VP cores, the micelles coated TEM grids were then exposed to I_2 vapor (Iodine, >99.8%, Sigma-Aldrich) for 3 hours at room temperature, by placing iodine crystals and TEM grids in a sealed glass container.(109)

4.2. Using Raman spectroscopy to identify the different phases in the iron oxide nanoparticles under different annealing conditions

Given the different crystal structures of the Fe_xO_y polymorphs, the vibrational modes and Raman spectra of different phases of iron oxide nanoparticles,(110) thin films,(111) particle aggregations,(112) and bulk solids(113) can be easily identified. Using group theory, the active Raman modes of a system can be predicted. The γ – Fe_2O_3 with the *$P4_{1g}32$* space group has five (A_{1g}, E_{1g} and 3 T_{2g}), mathematically describing their atomic vibrations against their rotational principle axis and inverse structures. Though γ – Fe_2O_3 and Fe_3O_4 belong to the same space group, the observed Raman phonons at similar wavenumber have a different atomic origin, making them easily distinguishable.(112,114) Raman can as well readily determine the purity of the crystallographic phase in the particles under various conditions,(114–116) as α-Fe_2O_3 with *R3c* space symmetry possesses seven Raman active modes (2 x A_{1g} and 5 x E_g) that are clearly distinguishable. Raman is also capable of differentiating the hydrogenated $FeCl_3$ species(99,116) and peaks shifting induced by laser illumination for α-Fe_2O_3.(117) As well, the Raman spectra for PS-P2VP has been reported (118,119) with modes mostly in the higher wavenumber regime, which do not interfere with the iron oxide modes. When $FeCl_3$ complexates with the P2VP block inside the micelles, it induces two Raman modes due to the steric hinderance of Fe-2VP complexation.(110) Table 4.1. summarizes the characteristic peaks positions for $FeCl_3$ (iron precursor salt), hematite, and maghemite. For Raman sample preparation, KBr substrates were employed as its Raman features do not interfere the features of the materials in this study.

Table 4.1. Expected Raman peaks for $FeCl_3$, Fe_3O_4 and different phases of Fe_2O_3

$FeCl_3$(98,99, 120,121)	**α – Fe_2O_3** (122)	**γ – Fe_2O_3**(111)
	225	
	247	
282	293	
330*		
		365
	412	
	498	511
	613	
		700

*Hydrated $[FeCl_4]^-$

In the search for the best magnetic iron oxide nanoparticles for optical isolation, we examined different annealing conditions with two diblock co-polymers. The Raman spectra from both polymers (P4824 and P9861) are summarized in Figure 4.1 from (i) to (viii). The exact polymers used, and annealing conditions are summarized in Table 4.2.

Starting from Figure 4.1 (i), five distinct peaks can be observed. Three can be assigned to the symmetric double-degenerate E_g modes 292 cm^{-1} (vibrations due to Fe atoms), 409 cm^{-1} (vibrations of O ions with respect to the Fe ions in the plane perpendicular to the c-axis of the hexagonal unit cell) and 613 cm^{-1} of α-Fe_2O_3. The two additional E_g modes are typically not observable when Raman spectra are collected at room temperature.(111,122,123) The other two peaks of α-Fe_2O_3 at 223 cm^{-1} and 497 cm^{-1} could be assigned to the A_{1g} stretching modes due to the vibrations of Fe ions moving along the c-axis of the hexagonal unit and O ions moving along the c-axis of the hexagonal unit cell respectively(122,123). By changing the annealing conditions and polymer, we can see that the spectra changes. In Fig. 4.1(ii), there can be observed the emergence of a new peak around 660 cm^{-1}. Though this could be the IR active longitudinal optical E_u mode activated by disorder, (111,115,124) it also could correspond to the emergence of the broad peak around 700 cm^{-1} of γ – Fe_2O_3. Further modification of the combination of diblock copolymer and annealing shows further evidence of the emergence of γ – Fe_2O_3, culminating in the Figure 4.1 (vii) where only three peaks can be observed. The broad peak around 700 cm^{-1} could be fitted with two Lorentzian fits at 670 and 720 cm^{-1}. This peak represents the A_{1g} stretching mode of tetrahedral units in γ – Fe_2O_3 (113,125). The peak at 509 cm^{-1} could be assigned to the E_g mode of γ – Fe_2O_3, which represents the symmetric bands of O with respect to Fe. The broad peak at around 360 cm^{-1} is assigned to the transalatory T_1 mode of γ –Fe_2O_3 which was fitted using two Lorentzian fits at 345 cm^{-1} and 384 cm^{-1}. The observed peaks for each spectrum are summarized with their assignment in Table 4.3.

Due to the presence of features from both the γ – Fe_2O_3 and α-Fe_2O_3 phases in the same spectrum, we used the intensity ratio of the A_2 peak of γ – Fe_2O_3 (~550-800cm^{-1}) against the A_2 of α-Fe_2O_3 (~150-300cm^{-1}) to make a semi-quantitative estimate of the percentage of each phase, following a modified approach similar to that by Bersani et al.(115) and Chuorpa et al.(113) As Raman is more sensitive to the α-Fe_2O_3 phase, this is probably an underestimation of the amount of γ – Fe_2O_3 present in the samples. Though the Raman analysis was not correlated to the XRD data, it was used here to provide a semi-quantitative analysis of the relative abundance of each phase.

To calculate the intensity, the area of the A_2 peak of the α phase at 223 cm^{-1} and the area of the A_2 peak of the γ phase at 700 cm^{-1} were approximated using the rectangle approximation with widths of approximations as small as 2cm^{-1}.

The area intensity ratio of γ phase to α phase was given by $\Sigma = \frac{I_\gamma}{I_\alpha}$.

The percentage of γ phase to α phase was given by $\%\gamma = \frac{\Sigma}{\Sigma+1} * 100$.

Following this approach, the %γ of the nanoparticles resulting from the conditions of Figure 4.1 (ii) is 28%, and for Figure 4.1 (vii) is 94%. The approximate percentage of γ – Fe_2O_3 for each processing condition is summarized in Figure 4.1 (b).

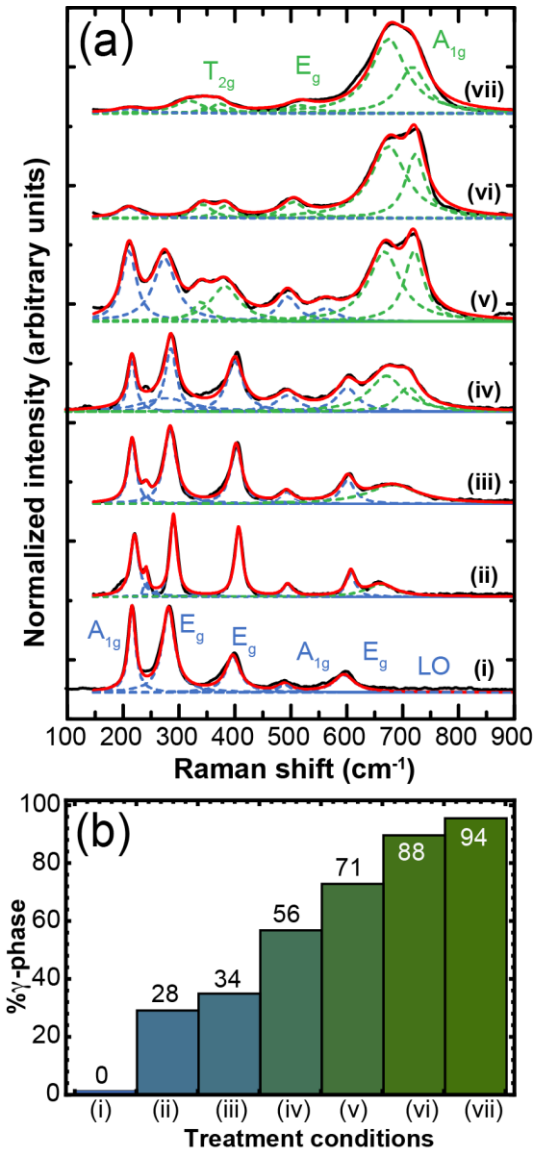

Figure 4.1. Normalized Raman spectra of the iron oxide nanoparticles synthesized by the reverse micelles method under various annealing conditions with Lorentzian line peaks fitting. (b) Percentage of γ- phase determined from the Raman spectra for each annealing condition

Table 4.2. Polymers used and annealing conditions for each step.

Figure	Polymer used	Annealing conditions
(i)	P9861	600°C, N_2 for 2h
(ii)	P4824	600°C, N_2 for 2h + 600°C, Air for 2h
(iii)	P9861	600°C, N_2 for 1h
(iv)	P9861	350°C, N_2 for 1h
(v)	P4824	600°C, N_2 for 2h + 600°C, Air for 6h
(vi)	P4824	600°C, N_2 for 2h
(vii)	P4824	350°C, N_2 for 12h + 350°C, Air for 12h

Table 4.3. Table of observed Raman peaks and their assignments.

Observed Raman shift (cm^{-1})	Related spectra in Figure 4.1	Assignment	References
214	(v)	A_{1g} of α-Fe_2O_3	(85,88)
219	(i), (iii), (iv)	A_{1g} of α-Fe_2O_3	(85,88)
243	(ii), (iii), (iv)	E_g of α-Fe_2O_3	(85,88)
277	(v)	E_g of α-Fe_2O_3	(85,88)
284	(i), (iii)	E_{1g} of α-Fe_2O_3	(83,84)
288	(iv)	E_g of α-Fe_2O_3	(85,88)
292	(ii)	E_{1g} of α-Fe_2O_3	(83,84)
345	(vii)	T_{2g} of γ – Fe_2O_3	(86)
385	(v), (vi)	T_{2g} of γ – Fe_2O_3	(86)
409	(ii), (iii), (iv)	E_g of α-Fe_2O_3	(85,86)
497	(i), (ii), (iii), (iv), (v)	A_{1g} of α-Fe_2O_3	(85,86)
610	(i), (ii), (iii), (iv)	E_g of α-Fe_2O_3	(85,86)
663	(ii), (iv)	LO Eu of γ – Fe_2O_3	(86)
677	(vii), (vi), (v), (iii)	A_{1g} of γ – Fe_2O_3	(68,88,89)
725	(vii), (vi), (v), (iv)	A_{1g} of γ – Fe_2O_3	(68,88,89)

As Figure 4.1 (b) shows, by changing the polymer and the annealing conditions, it is possible to change the ratio of γ – phase to α – phase in the nanoparticles. This is critically important information for the production of magnetic nanoparticles as the α – phase is anti-ferrimagnetic, and will likely poison the magnetic properties. For applications requiring highly magnetic particles, we would desire nanoparticles with the highest percentage of γ – phase Fe_2O_3. Annealing at 350°C, N_2 for 12h + 350°C, Air for 12h using P4824 for the micelles yielded 94% γ – phase, which was the highest percentage that we could achieve using the conditions tested. However, there are other applications where the tunability of the iron oxide crystal phase is of interest, including nanoparticles for sensors, photocatalysts, or batteries.

4.3. Identifying the differences between P9861 and P4824

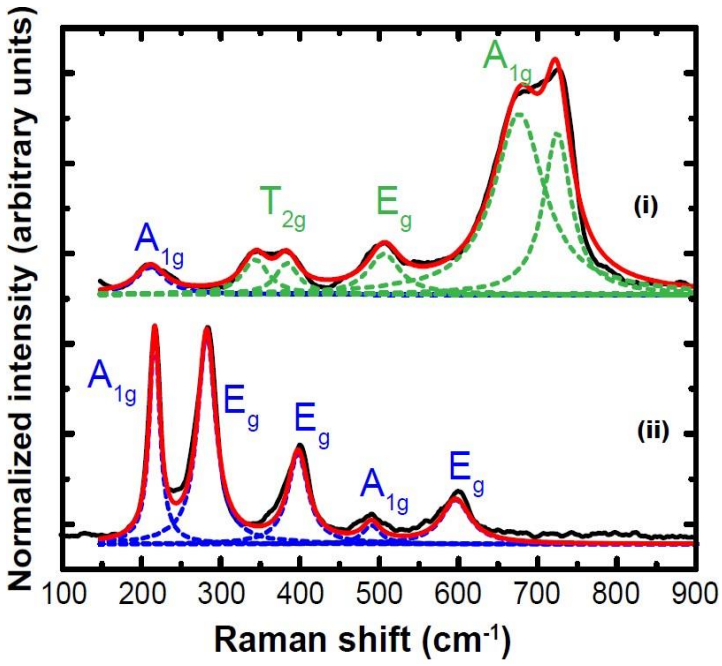

Figure 4.2. Raman spectra of the iron oxide nanoparticles synthesized by the reverse micelles method under the same annealing conditions with peaks fitting. (i) P4824 annealed at 600°C under N_2 environment for 2h; (ii) P9861 annealed at 600°C under N_2 environment for 2h. The spectra were fitted with Lorentzian peaks.

Figure 4.2 shows the iron oxide nanoparticles synthesized by two different diblock copolymers, (i) shows P4824 while (ii) shows P9861. The same annealing conditions were applied for both which was 600°C under N_2 environment for 2 hours. For (i), the broad peak around 700 cm^{-1} could be fitted with two Lorentzian peaks at 670 and 720 cm^{-1}. This peak represents the A_{1g} stretching mode of tetrahedral units in γ – Fe_2O_3.(113,114,125) The peak at 509 cm^{-1} could be assigned to the E_g mode of γ – Fe_2O_3, which represents the symmetric bands of O with respect to Fe. The broad peak at around 360 cm^{-1} is assigned to the translatory T_1 mode of γ – Fe_2O_3 which was fitted using two Lorentzian fits at 345 cm^{-1} and 384 cm^{-1}.(111,113,114) There is also evidence of a small peak at 213 cm^{-1} which is assigned to the A_{1g} mode of α-Fe_2O_3.(111,122,123) These peaks indicate that using the P4824 polymer for reverse micelle deposition of iron oxide from $FeCl_3$ has resulted in iron oxide nanoparticles that are most in the γ – Fe_2O_3 form; from our peak comparison, we estimate about 88% γ – phase. However, if the diblock copolymer is changed to a low molecular weight version, with similar PS:P2VP ratio, under the same annealing conditions, a completely different Raman spectrum can be observed. The spectrum from Figure 4.2 (ii) are characteristic of α-Fe_2O_3, with no evidence of γ – Fe_2O_3. Three E_g modes are resolved (292 cm^{-1}, 409 cm^{-1}, and 610 cm^{-1}); the two other peaks at 223 cm^{-1} and 497 cm^{-1} can be assigned to the A_{1g} modes of α-Fe_2O_3.(111,122,123) There is a complete absence of any

peaks from the γ – phase. To explain this behaviour, we have examined the loading behaviour of $FeCl_3$ prior to plasma etching.

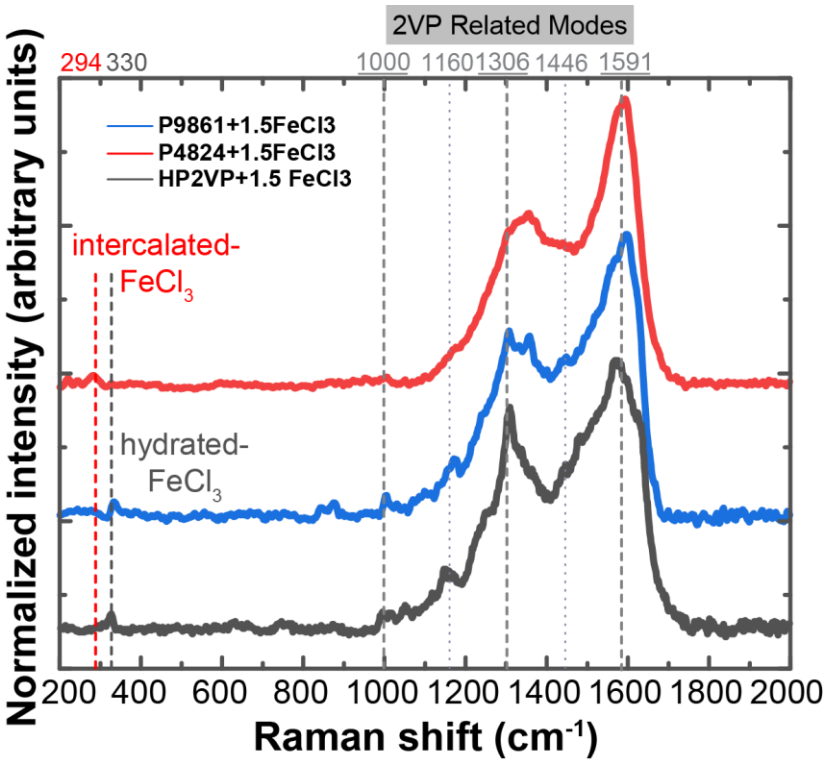

Figure 4.3. The Raman spectra of the different loaded micelles of P4824 and P9861. P9861 with a loading ratio (LR) 1.5 (blue).,P4824 with a LR 1.5 (red), homopolymer of P2VP with 1.5 LR (black)

Recently, Liang et al.(110) identified three features of $FeCl_3$ loaded micelles which are characteristic of the complexation of $FeCl_3$ and 2-vinylpyridine (2VP). The two pyridine related stretch modes at 1306 and 1575 cm^{-1} are enhanced due to the resonant interaction of Fe with the unpaired electrons of N on the pyridine rings; simultaneously the ν(1) symmetric ring breathing mode of P2VP at 1000 cm^{-1} is suppressed. Additionally it was observed that when $FeCl_3$ was infiltrated inside the micelle, a peak at around 290cm^{-1} emerged related to the intercalation of $FeCl_3$ and P2VP.(110) As seen in Figure 4.3, for the two different polymers, as well as a homopolymer of 2VP, there is evidence of Fe-2VP complexation, with large resonant peaks at 1306 and 1575cm^{-1}, and suppression of the 1000cm^{-1} peak. For the P4824 polymer, the intercalation peak for $FeCl_3$ is visible at 294cm^{-1} (red), assigned to the A_{1g} mode of pristine $FeCl_3$.(110,120,121) Though the P9861-$FeCl_3$ mixture shows a low wave number peak related to $FeCl_3$ similar to the P4824, the peak is extremely red shifted to 330cm^{-1}. This can be assigned to the hydrated $FeCl_3$ A_1 mode.(98,99) A similar behaviour was observed for the homopolymer loaded with $FeCl_3$, as seen in Figure 4.3. The $FeCl_3$ salts are, upon deposition, exposed to water adsorbed on the KBr substrate when complexated on the homopolymer HP2VP chain. As $FeCl_3$ is highly hygroscopic, it immediately forms a hydrated phase (this is also observed when $FeCl_3$ is deposited directly on the KBr surface(110)). Moreover, when homopolymer loaded $FeCl_3$ or

pure $FeCl_3$ is plasma etched, only characteristic peaks for the α-Fe_2O_3 phase can be observed. Direct formation of iron oxide nanoparticles from $FeCl_3$ solutions without micelles have noted the formation of intermediate iron hydroxides that can ripen into α-Fe_2O_3.(126) The formation of a hydrated phase therefore seems to be an intermediate requirement for the formation of α-Fe_2O_3 at low temperatures. This additionally suggests that the P4824 micelles provide a shielding environment for salts infiltrated inside, but the P9861 does not provide a shielding environment, similar to the case when the homopolymer alone is deposited on the KBr surface. This allows for moisture to combine with the $FeCl_3$ salts which are highly hygroscopic.

An analysis of the two different micelles allows us to develop a model of the different behaviour of the salt with the different micelles. Table 4.4 compares the properties of the two different micelles.

Table 4.4. Comparison between P4824 and P9861.

	P4824	P9861
P2VP:PS ratio	0.89	1.28
P2VP M_N (x 10^3)	66.5	36
PS M_N (x 10^3)	75	28
Micellar Diameter (nm)	41.12 ±3.64	94.57 ± 4.01
Core Diameter (nm)	30.86 ±4.10	74.66 ± 3.92
Corona Thickness (nm)	5.13 ±2.74	9.96 ±2.80
Micelle centre height (nm)	9.54±1.12	8.12+0.95
Micelle Core Young's Modulus (GPa)	2.24 ±0.05	0.17 ± 0.07

As can be seen from table 4.4, the two polymers have very different molecular weights for the P2VP to PS blocks, which results in very different block lengths in the final micelle structures. Though micelle size is expected to decrease with the molecular weight of the polymer chains,(127–130) we can see from Table 4.4 that the average micelle diameters, as measured by SEM, were substantially larger for P9861 compared to P4824. When we compare the SEM results to the AFM images seen in Figure 4.4(a) and (b) (line profiles shown in Figure 4.4(e) and (f)), we observe a similar radius. However, the micelle height noted in shows a micelle height of 8 nm, almost identical or slightly smaller than that for P4824.

We used iodine staining to determine the inner core radius, as iodine is known to preferentially stain pyridine over polystyrene.(131) Typically in SEM/TEM, empty micelles have very low contrast due to the weak elastic interactions of carbon and nitrogen with energetic electrons, without a significant difference for PS and P2VP blocks. By exposing the empty micelles to an iodine vapor, the P2VP cores can be made visible due to the preferential complexation of iodine and pyridine.(132) Using the difference in the measured micelle and core diameters, the thickness of the PS corona can also be estimated to get an idea of the size and shape of the resultant micelles. This analysis indicates that the P2VP core is smaller in the case of P4824,

with the micelles densely packed. On the other hand, the P9861 is twice the size, even though the length of the polymer chains are much shorter, due to the lower molecular weight of the polymer.

We used quantitative nanomechanical property mapping (QNM) using the AFM in tapping mode to examine the properties of the micelles(107). QNM allows the measurement of the Young's modulus variation on a surface, and has been successfully applied to examining the properties of soft materials.(133–135)

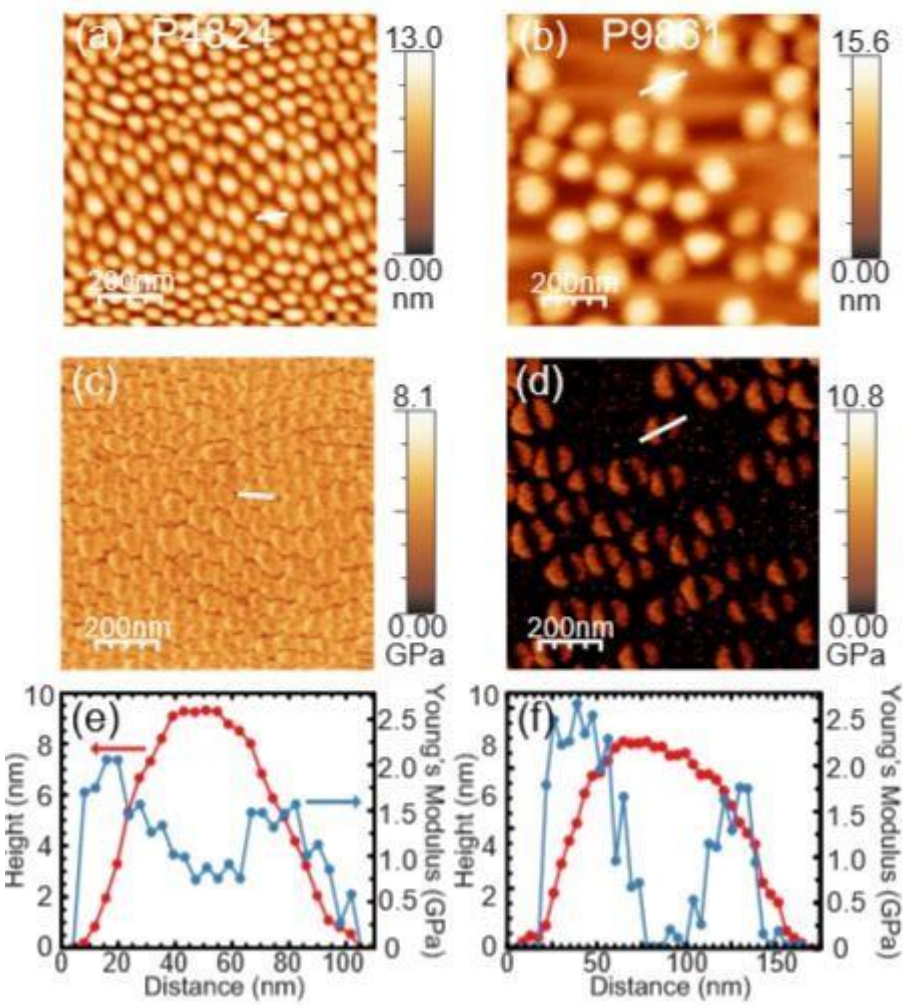

Figure 4.4. (a) AFM topography images of the P4824 micelles deposited on Si (b) AFM topography image of P9861 micelles deposited on Si (c) Corresponding Young's modulus image of P4824 (d) Corresponding Young's modulus image of P9861 (e) Line profile for the P4824 micelles (f) Line profile for the P9861 micelles

As seen in Figure 4.4(e), the line profile through the empty micelle P4824 indicates that the measured Young's modulus of the core is slightly less than the corona region. This lowering of the modulus through the core likely results from anisotropic nature of polystyrene in the diblock copolymer. The diblock copolymers are aligned horizontally when the tip first interacts

with the micelle and vertically as the tip interacts with the core; as the polystyrene has a higher Young's modulus when aligned laterally in a lamellar formation than vertically as in a polymer brush, the modulus is reduced through the core.(135) On the other hand, P9861, as Figure 4.4(f) shows, has a strong Young's Modulus in the corona region, similar to that observed for P4824, but goes to zero at the center with respect to the silicon substrate. This results in a “coffee bean” type structure, as seen in Figure 4.4(d) and (f) for P9861 micelles.

For P9861, the small height of 8 nm, accompanied with an extreme decrease in Young's modulus, seemingly indicating that the micelle has collapsed when it was deposited on the Si surface. We believe that these micelles balloon out in solution due to the interaction with the solvent but collapse when they are deposited and the solvent evaporates.

This behaviour can suggest a mechanism by which the P9861 polymer is not able to protect the $FeCl_3$ precursor during the plasma etching. In the typical process of nanoparticle formation using micellar templates, micelles will form spontaneously in selective solvents when there are enough diblock copolymer unimers to be above the critical micelle concentration. In non-polar solvents such as o-xylene or toluene which selectively dissolves polystyrene, PS-P2VP forms reverse micelles as shown schematically in Fig. 4.5, where the hydrophillic P2VP block forms the micelle core surrounded by a hydrophobic corona of PS.

The spherical structure consists of loosely associated unimers, which are very dynamic with unimers regularly exchanging between the micelle and the solvent.(136–138) The size and shape of the micelles in solution is driven by the molecular weight of the polymer chains and their interaction with the surrounding solvent. In the case of P4824, the longer P2VP chains are packed tightly together, forming a dense 2VP core inside the micelle, and closer packed PS. On the other hand, for P9861, the shorter chains are stretched, and the micelle balloons out.

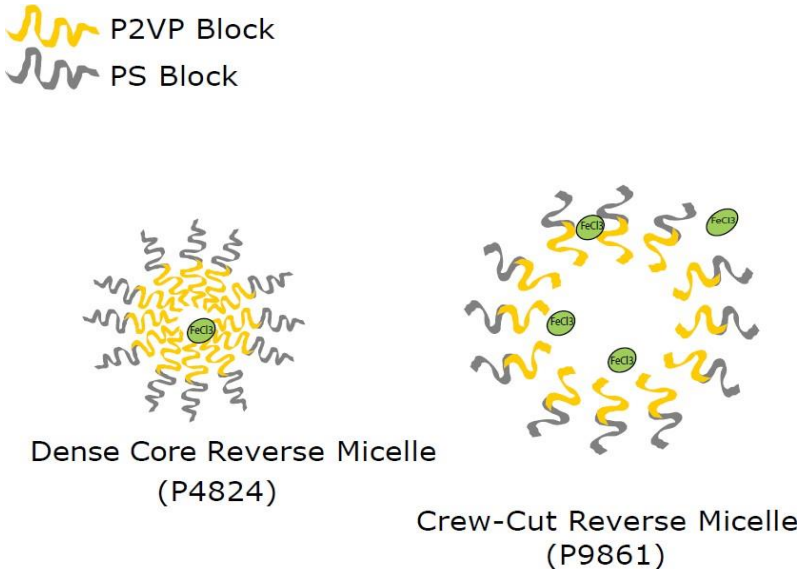

Figure 4.5. Schematic of the structure and interaction of $FeCl_3$ -loaded micelles from the two polymers.

In both cases, the dynamic nature of the micelles allows the $FeCl_3$ to penetrate through the corona due to the osmotic pressure of the non-polar solvent. Driven by the incompatible polarity between non-polar solvent and the polar metal salt, the precursor ions diffuse into the micellar cores. Once inside, the $FeCl_3$ then interacts with the P2VP chains. As explained in chapter 5, the loading ratio required to produce the same size nanoparticles with P4824 and P9861 are very different. In the dense environment of the P4824 micelle, a loading ratio of 1.5 is required to produce particles with an average diameter of ~20nm. It is relatively difficult for the $FeCl_3$ to penetrate inside the dense micelles, but once inside it is protected by both the PS and the P2VP unimers, which do not collapse when the solvent evaporates after deposition. This allows the $FeCl_3$ to be protected from water in the environment, preventing it from turning into a hydrated salt (as shown by the $FeCl_3$ peak at 293cm^{-1} in Figure 4.3). Upon plasma etching, due to the low temperature and the lack of a hydrated salt, the γ – phase is able to form.

On the other hand, the large balloon-like micelles of P9861 allow easy infiltration of the salt while in the solution. To achieve ~20 nm nanoparticles, P9861 only requires a LR of 0.2. This suggests that a large amount of $FeCl_3$ is able to penetrate inside the micelle, some of which interacts the P2VP. However, when the micelle is deposited on the surface, the micelle collapses and is not able to protect $FeCl_3$ precursor properly, causing it to turn into hydrated $FeCl_3$ (with a peak observed at 330cm^{-1} in Figure 4.3). Due to the presence of this hydrated phase, it is extremely easy to form the α – Fe_2O_3 phase.

4.4. Summary

In summary, in this chapter we discussed the behaviour of iron oxide formation using different diblock copolymers using Raman spectroscopy. The nanoparticles were synthesized using the reverse micelles method. We were able to identify and tune the exact phase of iron oxide using different treatments. Using different polymers, post-deposition annealing temperatures and times, we could produce pure α – Fe_2O_3 nanoparticles, almost pure γ – Fe_2O_3 nanoparticles, and mixed phases with varying percentage of γ – Fe_2O_3. Moreover, we were able to understand why P4824 is capable of protecting the precursor salt better yielding higher degrees of crystallinity and hence better magnetic response. This is extremely useful as the nanoparticles synthesized by P4824 has a higher chance of yielding γ – phase which is what we need in order to have a successful optical isolator. The full discussion on integrating the iron oxide nanoparticles on silicon waveguides to achieve isolation will be discussed in Chapter 7.

Chapter 5

Optimization of monolayer iron oxide nanoparticles

Raman characterization was carried out in the last chapter however, other techniques were required to understand the monolayer iron oxide nanoparticles by themselves instead of the thick layer as the dropcasted Raman sample. An important feature of the nanoparticles that influences magnetization is size, therefore different loading ratios were deployed in an attempt to have different sizes for the nanoparticles. AFM was used to showcase the topography of the different loading ratios. In addition, the magnetic properties of the monolayer iron oxide nanoparticles were studied by using SQUID.

Moreover, we also show the difference between both polymers and the effects of using P4824 and P9861 on the particles' size and magnetic properties using AFM and SQUID respectively.

As our goal is to apply the magnetic nanoparticles on the silicon waveguides to achieve optical isolation, a deep understanding of the different loading ratios and different polymers will help us choose the best loading ratio and polymer to choose as the candidate to use on silicon waveguides. We have already established the best annealing conditions from chapter 4 using Raman.

5.1. Experimental

The $FeCl_3$ loaded micelles and iron oxide nanoparticles were synthesized using the procedures described previously in chapter 3. Two different molecular weight polystyrene-block-poly (2-vinyl pyridine) (PS-bP2VP) were used in this experiment. PS-b-P2VP, M_n: 75000-b-66500, labeled as P4824 and PS-b-P2VP, M_n: 28000-b-36000 labeled as P9861. The diblock copolymer was dissolved in o-xylene above the critical micelle concentration. The polymers were dissolved in o-xylene to produce 3.00mg/ml solutions respectively. After spinning for 24 hours, the micelles solutions were spin coated on the 1 by 1 cm silicon substrates. The spin coating speed was set to 45 seconds at 2000 RPM.

Similarly, the iron oxide nanoparticles were synthesized following the procedures from chapter 3. The loading ratio "LR" (number of Fe^{3+} ions divided by the number of 2VP molecular units in PS-bP2VP) was set to 0.2 and 1.5 to test the different loading ratios.

The above micelles or iron oxide nanoparticles were characterized on silicon using AFM to obtain the topographic information. WSxM was used to extract the AFM raw data (76).

SEM was used to characterize the nanoparticles' size, the substrates for SEM characterization were Pdoped silicon wafers with thickness of 380µm, orientation of <100> and resistivity: 0.001-0.005 ohm-cm.
These wafers are conductive enough to allow the direct SEM imaging of nanoparticles without coating. The nanoparticles coated substrates were mounted by carbon tape and nickel paste on 25.4mm standard Al stubs. The SEM characterizations were conducted in FEI Versa 3D SEM with a Schottky thermal field emitter electron gun. The accelerating voltage and probe current were normally adjusted to 5kV and 12pA to minimize the charging effect, which still maintained good signal-to-noise ratio for high quality imaging.

For magnetic properties measurement, the silicon samples were created using the procedure described in chapter 3. All SQUID samples were treated with 25 minutes oxygen plasma before annealing. To investigate the size effect on the magnetization, two different solutions (0.2 LR" Loading Ratio" $FeCl_3$ and 1.5LR $FeCl_3$) were used to produce different average size of iron oxide nanoparticles with the same annealing conditions (350°C for 12h in Air followed by 12h in N_2).

5.2. Iron oxide nanoparticles size analysis using different loading ratios and different polymers

The size of the iron oxide nanoparticles is directly related to the loading ratio of the $FeCl_3$. The two loading ratios were set to have a nanoparticle size that was less than the single domain limit defined as:

$$D_{single} \sim 36 \frac{\sqrt{A * K_{eff}}}{\mu_0 * {M_s}^2}$$

The single domain diameter limit was calculated in chapter 2 and was found to be around 50nm. The loading ratios were chosen to have a particle size closer to the single domain limit which is the 1.5 loading ratio compared to the standard loading ratio of 0.2 for $FeCl_3$. However, studies on the relationship between particle size and magnetic properties specifically saturation magnetization, remanence and coercivity remain sparse. Smolensky (139) revealed that 18 nm particle size results in higher saturation magnetization and higher coercive field than 7 nm. This is the bases of our study for this chapter by increasing the size; we expect higher magnetic response.

The loading ratio (LR) is defined as the ratio between Fe^{3+} ions and 2VP is used to calculate the amount of $FeCl_3$ to add:

$$\frac{n(\mathrm{Fe3+})}{n(2VP)} = 0.2$$

$$\frac{n(\mathrm{Fe3+})}{n(2VP)} = 1.5$$

Moreover, changing the molecular weight of the diblock copolymer directly impacts the aggregation number (the number of the diblock copolymer molecules that make up the micelle) which influences the core and the corona size of the micelle (57). To study this effect, two different molecular weights of PS-b-P2VP P4824 and P9861 were used.

The different loading ratios yield different nanoparticles sizes as Figure 5.1 shows, Figure 5.1(a)&(b) show the different loading ratios yielding larger particle sizes in the case of the 1.5LR for P4824. The 1.5LR has shown to yield micelles that are closer together and not necessarily a monolayer array of iron oxide nanoparticles. After 25 minutes of etching, as 5.1(e) shows the particles are still very clustered. In the P4824 1.5LR, the particles have very small interparticle distance compared to the P4824 0.2LR. Figure 5.1(c) shows the etched particles of 0.2LR, the particles have a smaller size than both P4824 1.5LR, with an intermediate interparticle distance.

Figure 5.1 also presents the AFM topography image of the micelles array from P9861 0.2LR. By comparing the images, we can see that P9861 loaded micelles have a similar size to the P4824 1.5LR loaded micelles. However, post etching we can see that the particles are more dispersed and have larger interparticle distance. Moreover, the P9861 nanoparticles post etching do not yield spherically shaped nanoparticles as the P4824 0.2LR. Table 5.1 summarizes the heights for the different images from figure 5.1 supporting that 0.2 LR P9861 and P4824 1.5LR yield comparable particles' sizes.

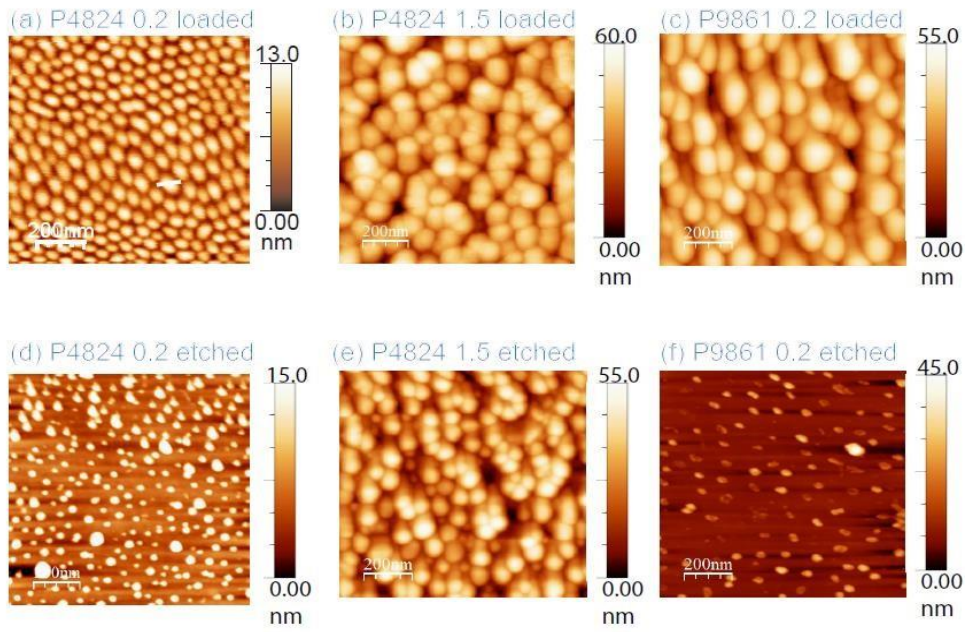

Figure 5.1. AFM topography images of (a) P4824 0.2 loading ratio loaded $FeCl_3$, (b) P4824 1.5 loading ratio loaded $FeCl_3$, (c) P9861 0.2 loading ratio loaded $FeCl_3$, (d) P4824 0.2 loading ratio post etching, (e) P4824 1.5 loading ratio post etching, (f) P9861 0.2 loading ratio post etch

Table 5.1. Table of observed particles heights and standard deviation using different polymers and different loading ratios

	Height (nm)	**Standard deviation**
P4824 0.2 loaded	11.31	3.12
P4824 1.5 loaded	48.41	3.15
P9861 0.2 loaded	45.86	2.98
P4824 0.2 etched	8.89	2.82
P4824 1.5 etched	44.12	4.14
P9861 0.2 etched	38.28	4.97

Moreover, Figure 5.2 shows the SEM dispersion and size comparisons for the P9861 0.2LR and P4824 1.5LR. The sizes as expected are very comparable, for P9861 the average size is 25.4 ± 4.1 nm and 28.3 ± 3.4 nm for P4824 1.5LR. This means that using P9861 for a smaller loading ratio can yield the same particle size as increasing the loading ratio in P4824, this is important as the overloading of $FeCl_3$ into PSb-P2VP has been reported to yield bad dispersion in the resultant nanoparticles(66,140). There exists a saturation limit for loading, above which the micelles structure is affected thus jeopardizing the control over size and dispersion of the nanoparticles (92,140). This ratio was found to be around 0.45 for P4824(141).

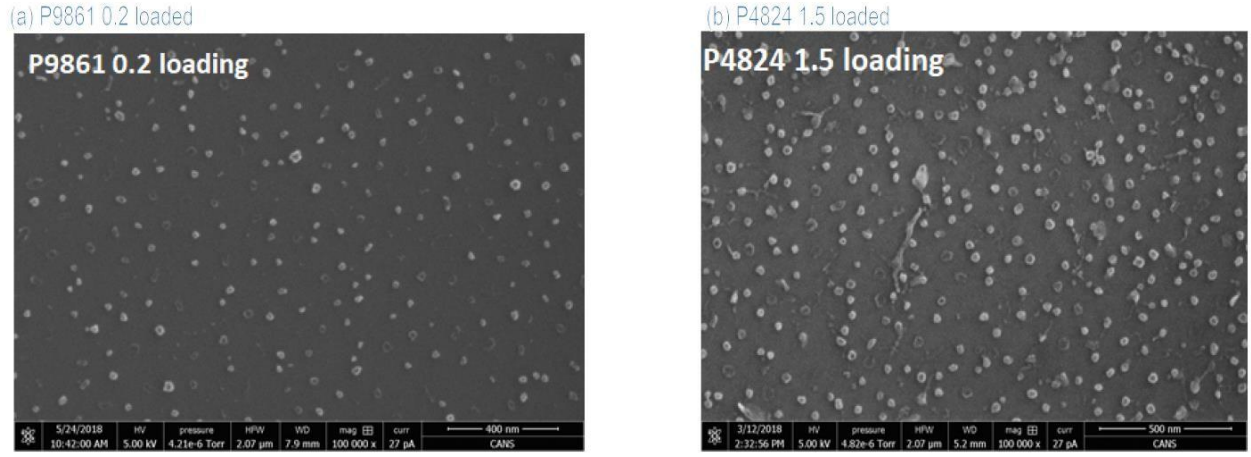

Figure 5.2. SEM dispersion and size comparison of (a) P9861 0.2LR and (b) P4824 1.5LR.

5.2.1. Magnetic properties of different loading ratios for iron oxide nanoparticles

In the previous section, we showcased the AFM topography of the different loading ratios and we were able to show the different heights and sizes of the iron oxide nanoparticles yielded by the different loading ratios and different polymers. However, the next step is using SQUID to measure the magnetic properties of both 0.2LR and 1.5LR for P4824 and P9861. Figure 5.2 shows the magnetic response of both the 0.2LR and 1.5LR at the same low temperature annealing conditions of 350°C for 12h in Air and 12h in N_2. This lower temperature annealing condition is applied to produce γ- Fe_2O_3 as described in chapter 4. Figure 5.3 shows the magnetization-applied magnetic field (M-H) curves of the nanoparticles after the annealing process.

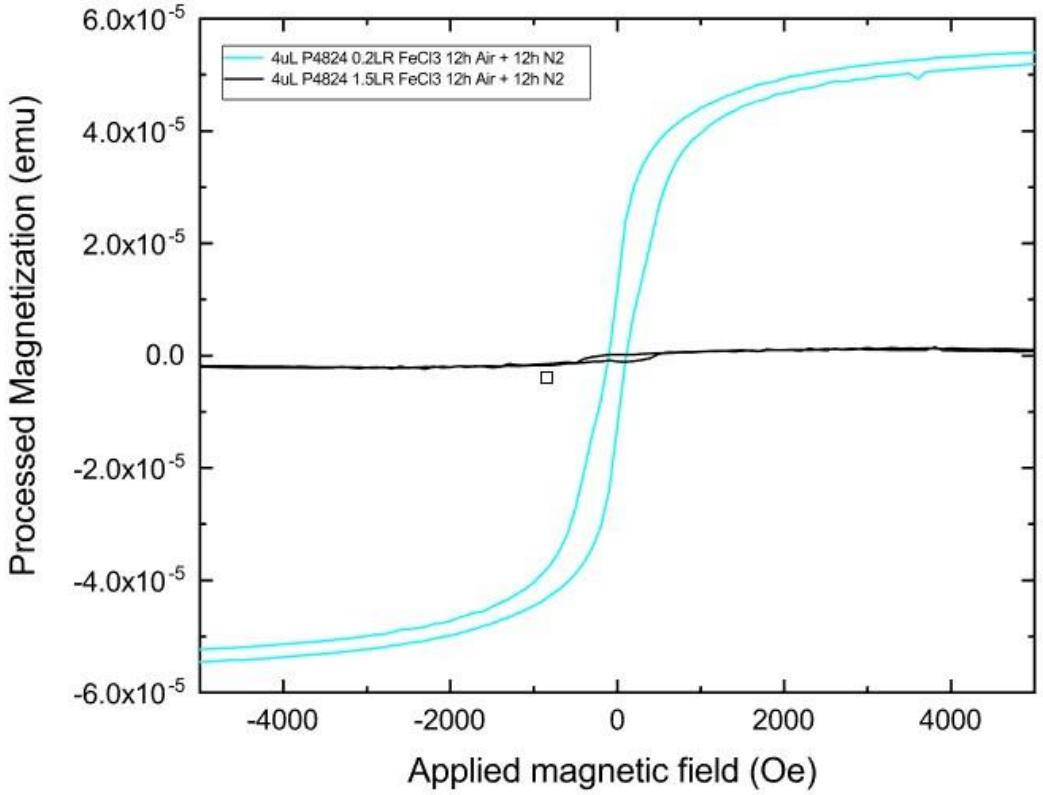

Figure 5.3. Magnetization-applied magnetic field curve of monolayer iron oxide nanoparticles on silicon substrates using both loading ratios after having the same annealing conditions of 350°C for 12h in Air and 12h in N_2.

The coercive field (H_c) was at around 100Oe for the P4824 0.2LR with the M_r in 10^{-5} emu region which accounted for 25% of the magnetization at 2000Oe, showing a clear hysteresis. However, for the 1.5LR we can see almost no magnetic response from the nanoparticles. This could be accounted as mentioned in the previous section that the interparticle distance is very small which causes the magnetization from each particle to cancel out having a very minimal response.

Moreover, we wanted to confirm that the magnetic response from the P4824 0.2LR is due to the high percentage of γ- Fe_2O_3 present as confirmed by chapter 4. We created another SQUID sample that was annealed at a different temperature (600°C for 2h in N_2). Figure 5.4 compares between the two samples discussed and the new sample.

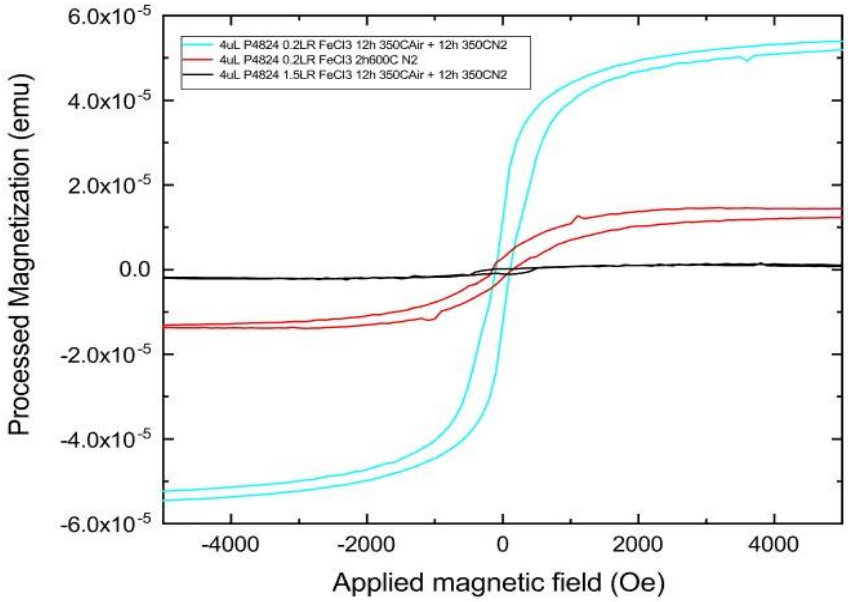

Figure 5.4. Magnetization-applied magnetic field curve of monolayer iron oxide nanoparticles on silicon substrates with different annealing conditions.

M_r for the 600°C is clearly lower in magnitude than the P4824 0.2LR under the low annealing process. This could be explained by the conversion of γ-Fe_2O_3 to α-Fe_2O_3 as supported by the Raman data from the previous chapter, reducing the magnetization due to the weak ferromagnetic nature of α-Fe_2O_3. Moreover, another sample was prepared and underwent two annealing process: 600°C annealing for 2h in N_2 and another 2h in air which was the same condition as Figure 4.1 (ii). In this case, the magnetic response was below the detection limit of the SQUID. This confirms that the higher the conversion of γ-Fe_2O_3 to α-Fe_2O_3 the worse the magnetic response will be. Moreover, we tried creating a sample that had 50% γ-Fe_2O_3 but that resulted in no response. On the other hand, temperature plays an important role as well as we saw in chapter 4 with the different annealing temperatures with the low temperature annealing process yielding mainly γ-Fe_2O_3. Thus, the low temperature annealing process at 0.2LR gives the best results in terms of magnetic response supported by the SQUID data. P9861 yields iron oxide nanoparticles that are mainly in the α phase as found by results in chapter 4, therefore, no SQUID data was done as the SQUID does not detect the α phase iron oxide nanoparticles.

5.3. Summary

In summary, we were able to conclude that the P4824 polymer with a loading ratio of 0.2 yield the best magnetic response for our desired functionality. We compared with a different loading ratio, then comparing two different polymers, comparing the size and the magnetic response.

Chapter 6

Tin oxide structure and properties and characterization

As concluded in chapter 5 we deduced that a specific loading ratio of 0.2 should be used with P4824. In this section, we explore a different metal salt to produce tin oxide nanoparticles. Tin oxide nanoparticles are very interesting and have been found to exhibit room temperature ferromagnetism(37). In this section, we explore the topography and magnetic properties of tin oxide compared with iron oxide nanoparticles.

6.1. Experimental

The $SnCl_3$ loaded micelles and SnO_2 nanoparticles were synthesized in the procedures that have been described in chapter 3. However, an extra step is added for the synthesis of SnO_2, after salt loading the $SnCl_3$ and waiting for 48 hours for it to mix properly with the diblock copolymer solution, 0.300 mL of ethanol is decanted and added to the solution. The mixture of $SnCl_3$, diblock copolymer, o-xylene, and ethanol is left to mix for an extra 48 hours before using. For this experiment, only one molecular weight polysterene-block-poly92-vinyl pyridine) PS-b-P2VP is used which P4824 (M_n: 75000-b-66500).

For magnetic properties measurement, SQUID was used to measure the magnetic properties of the SnO_2 nanoparticles. The full procedure for making the SQUID samples is explained in section 3.4.3.

The above micelles and tin oxide nanoparticles were also characterized by AFM to obtain the topographic information. WSxM was used to extract the AFM raw data(105).

6.2. AFM topography of Tin oxide nanoparticles

The AFM topography of the tin oxide nanoparticles synthesis process is shown in Figure 6.1. Figure 6.1 (a) shows the tin chloride loaded micelles, this is post the first step of synthesis after the salt $SnCl_3$ is loaded in the solution containing the P4824 solution. Figure 6.1 (b) shows the AFM topography image after the Ethanol loading, and then finally Figure 6.1 (c) shows after the plasma etching yielding tin oxide nanoparticles. The etched tin oxide nanoparticles have an average height of 48 nm, which is comparable to the 1.5 LR of $FeCl_3$ shown in chapter 5. The particles have a similar problem as the 1.5LR, which is the particles are clustered together.

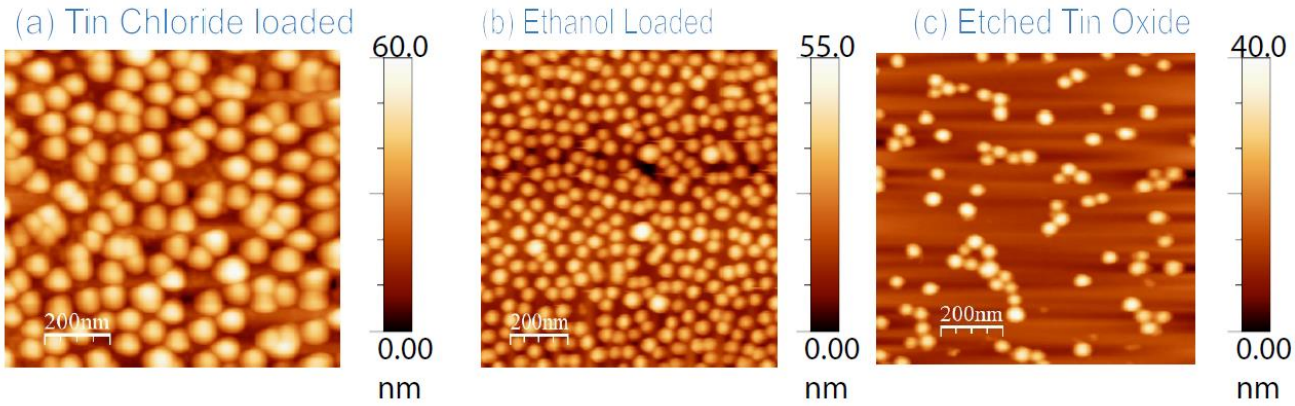

Figure 6.1. AFM topography images of (a) Tin chloride loaded micelles, (b) Tin chloride after loading with Ethanol, (c) Etched tin oxide nanoparticles

A SQUID samples was created and compared to that of P4824 0.2LR $FeCl_3$ SQUID sample used in chapter 5. The P4824 $SnCl_3$ sample annealed at 600°C in a N_2 environment for 2 hours. Figure 6.2 compares the AFM topography of both samples, Figure 6.2 (a) shows the AFM topography of the iron oxide nanoparticles created using P4824 with a loading ratio of 0.2. The particles have a better dispersion than that of the tin oxide nanoparticles' AFM image shown in Figure 6.2 (b). The tin oxide nanoparticles appear to be more clustered in specific areas on the silicon substrate, which ultimately could affect the SQUID results. The AFM topography is different for the SQUID samples for both the iron oxide and the tin oxide than the AFM previously shown due to the uneven width of the SQUID samples. The SQUID samples are 40 mm by 5 mm, with the solution spin coated on an area about 10 mm by 5 mm. This small uneven area can cause some of the solution dropped on the sample to fly off and thus yielding lower number of particles as shown in Figure 6.2.

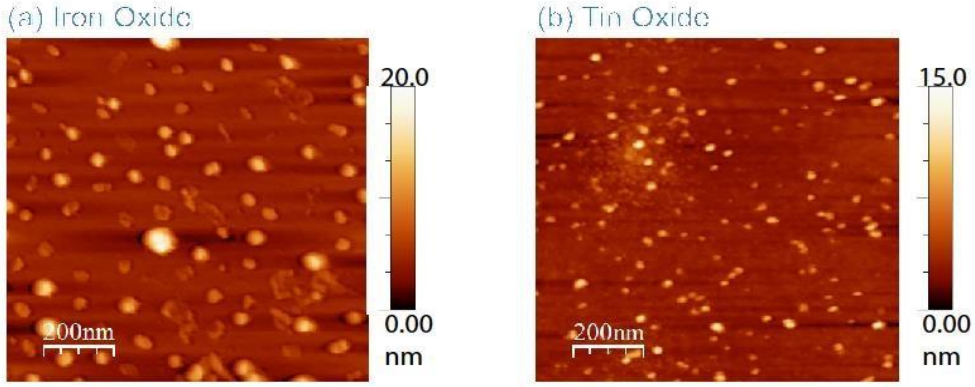

Figure 6.2. AFM topography images of SQUID samples of (a) Iron oxide nanoparticles, (b) Tin oxide nanoparticles

6.3. Magnetic properties of monolayer tin oxide nanoparticles compared to monolayer iron oxide nanoparticles under different annealing conditions

As we showed in the previous section, the AFM of the SQUID samples appear to favor the iron sample. However, we need to measure the magnetic response from both samples to be able to fairly compare between the tin oxide and iron oxide nanoparticles' magnetic response. Figure 6.3 shows the different iron oxide nanoparticles SQUID data shown in Figure 5.4 adding the tin oxide nanoparticles SQUID data. The figure shows the magnetization-applied magnetic field (M-H) curves of all the nanoparticles on silicon of the full annealing process to compare with the SnO_2 nanoparticles on silicon annealed at 600°C for 2h in N_2.

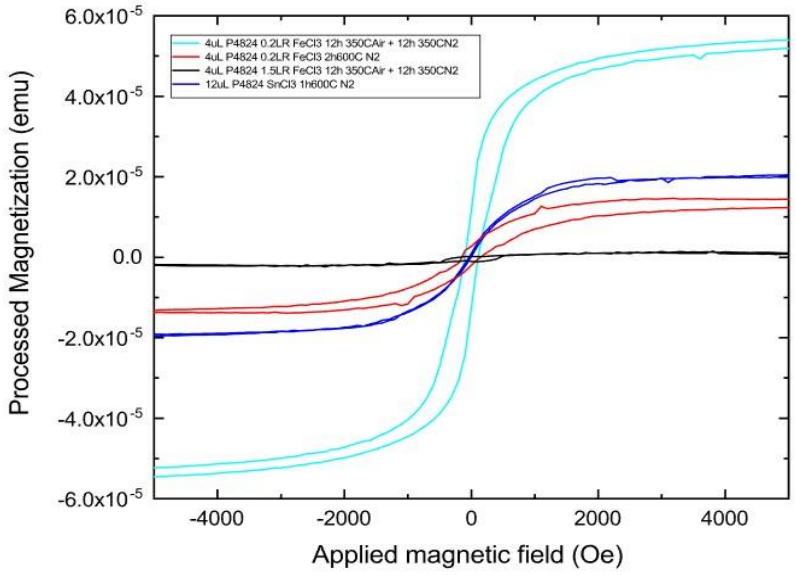

Figure 6.3. Comparison between the magnetization-applied magnetic field curves of monolayer iron oxide nanoparticles and tin oxide nanoparticles with different annealing conditions (92).

For the tin oxide nanoparticles, the coercive field (H_c) was around 40Oe with the remanence magnetization (M_r) was in the region of 10^{-7} emu. This accounts for about 6% of the magnetization at 2000Oe. The magnetic response from the tin oxide nanoparticles is clearly lower than the P4824 0.2LR $FeCl_3$ annealed at the low temperature annealing process, however, the magnetic response is better than the P4824 0.2LR $FeCl_3$ annealed at 600°C for 2 hours and the P4824 1.5LR $FeCl_3$ annealed at the low temperature annealing process.

Comparing the M-H curves results, we can confirm that the iron oxide nanoparticles possess the best magnetic properties when using low temperature annealing process, which yields higher purity γ-Fe_2O_3. However, more work needs to be done to achieve higher magnetic response from the tin oxide nanoparticles. Previous work shows higher magnetism by doping the tin (27), with low temperature annealing at 350°C. As well as, several authors have reported using different temperature annealing conditions (22,28) to synthesize tin oxide nanoparticles.

6.4. Summary

In summary, the tin oxide nanoparticles are very promising in terms of magnetic response compared to the different iron oxide nanoparticles SQUID data. However, more research needs to be done to be able to use tin oxide nanoparticles as optical isolators. For the time being, the best material to use as an optical isolator supported by chapters 5 and 6 is using P4824 with a loading ratio of 0.2 to create iron oxide nanoparticles, followed by a low temperature annealing process at 350°C for 12 hours in Air then another 350°C for 12 hours in N_2. This was proven to

show the best magnetic response supported by the Raman and SQUID data and thus, the best material to be used as an optical isolator.

Chapter 7

Optical Isolators and monolithically integration

In this chapter, we present preliminary results of an optical isolator using the magnetic nanoparticles synthesized in chapter 4 . We are utilizing the waveguide Faraday rotation phenomenon for our design. We will present the layout of the samples used for our proposed optical isolator.

7.1. Nanoparticle selection

In the previous chapters, we showcased iron oxide and tin oxide nanoparticles. For iron oxide, we tested two different polymers yielding different sizes of nanoparticles (P4824 and P9861). Then, we tested using different loading ratios to examine how the loading ratios affect the size and magnetization. After the different characterization techniques, we concluded that using P4824 with a loading ratio of 0.2 of $FeCl_3$ yielded the best magnetic nanoparticles. We concluded that P4824 0.2LR annealed using the low temperature annealing process yields higher saturation magnetization and better magnetic properties and thus, was chosen to be used in this chapter.

Dani et al.(6) proposed a model to describe the expected Faraday rotation for iron oxide nanoparticles coated by a gold shell and suspended in water as mentioned in chapter 2, the calculations were made over the ultraviolet region between 350 nm < lambda < 700 nm.

For the permanent magnetization in these single domain particles, the internal magnetic field is $H_{\text{in}} = -\frac{1}{3}M$ and the internal magnetic induction is $B_{\text{in}} = \mu_0(H_{\text{in}} + M) = \frac{2}{3}\mu_0 M$. The component along z is $B_{\text{in},z} = B_{\text{in}}\langle\cos\theta\rangle = \frac{2}{3}\mu_0 M\frac{x}{3} = \left(\frac{2}{9}\mu_0 VM^2/k_B T\right)B$. This internal magnetic induction is amplified by the factor $\left(\frac{2}{9}\mu_0 VM^2/k_B T\right)$ = 5.5, which helps to enhance the Faraday rotation compared to that in a non-magnetized medium. This calculation is done for nanoparticles with a radius of 4.85 nm.

Their calculations for maghemite coated with a gold shell shows that it can theoretically yield up to 10 rad/Tm for nanoparticles with an average radius of 4.85 nm in the UV region between 350 < lambda < 700 nm. Dani et al. only show results for the gold shell around the iron oxide core nanoparticles which they show that they experimentally yield Faraday rotation of 3 rad/Tm to 10 rad/Tm for a gold shell of 5nm coated on a 10nm Fe_2O_3 core measured at a wavelength of 632 nm.

However, the particles synthesized by our reverse micelles method have an average radius of approximately b = 10 nm for 0.2LR P4824. Thus, the volume of the particles is $V = 4\pi b^3/3$ = 1200 nm^3. This higher particles' volume results in a higher amplification factor for the internal magnetic induction by a factor of 3. The new amplification factor should be on the order of 15, expecting an even higher enhancement in the Faraday rotation. Theoretically, the larger radius nanoparticles should yield a higher Faraday rotation as long as the particles are in the single-domain limit for ferromagnetism.

7.2 Optical Isolator design

Figure 7.1 shows the GDS layout for the waveguide design that was used. The layout was designed, then sent to the University of Southampton to make a 3mm by 7mm silicon chip with the waveguide mask on top. The structures for testing are shown, all grating coupled so they are meant to be measured using cleaved fibers from above. Each waveguide can support both TE and TM modes, but the grating couplers only accept TE polarized light.

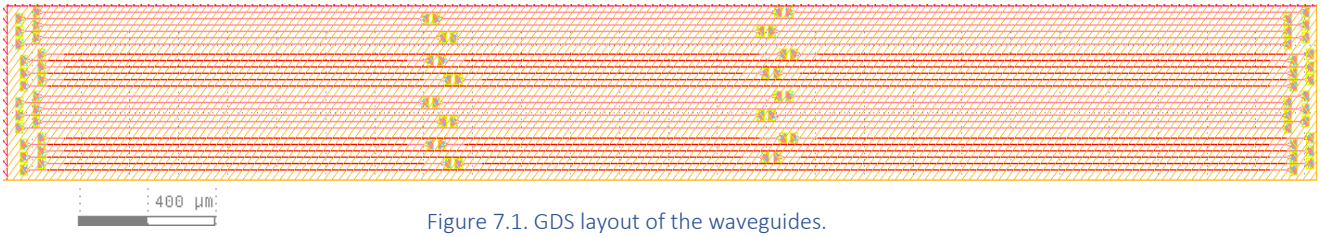

Figure 7.1. GDS layout of the waveguides.

The nanoparticles are deposited on top of the waveguides by spin coating as described in chapter 3, the particles are spin coated, etched for 25 minutes and then annealed using the low temperature annealing process at 350°C in air for 12 hours followed by 12 hours in N_2 at 350°C. Figure 7.2 shows a schematic of the iron oxide nanoparticles deposited on the waveguides. The figure shows an SOI waveguide, light is guided in a silicon core separated from the silicon substrate by an SiO_2 layer acting as the lower cladding.

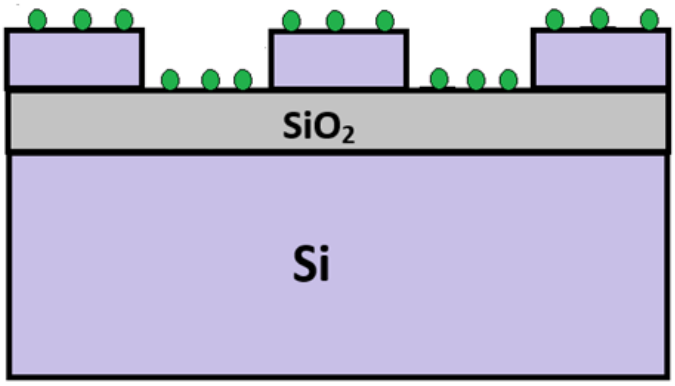

Figure 7.2. Schematic of the components required for a Faraday rotation waveguide isolator with the iron oxide nanoparticles.

To test the optical isolation of the iron oxide nanoparticles, we used the experimental setup outlined in Figure 7.3. Grating couplers ensure that light is propagating in TE mode. As the nanoparticles should work as a Faraday rotator, the light would be coupled from the TE to the TM mode as it propagates, and then it would not be able to exit the device, thus we should see a change in transmission as the magnet was brought closer and closer causing the nanoparticles magnetic moments to align. The magnet is set up to be as close as possible to the chip on the order of µm. The magnet used is a DIYMAG magnet, with a diameter of 32mm. The alignment of the magnet was set to be perpendicular to the direction of propagation of light, however, the alignment of the magnet was changed in an attempt to measure any change in transmission. The input laser wavelength was set to 1550 nm for all the chips. For optical communication, several wavelengths are used in the infrared region typically around 850, 1300 and 1550 nm. These wavelengths are used because the attenuation of the transmission is much less at those wavelengths.

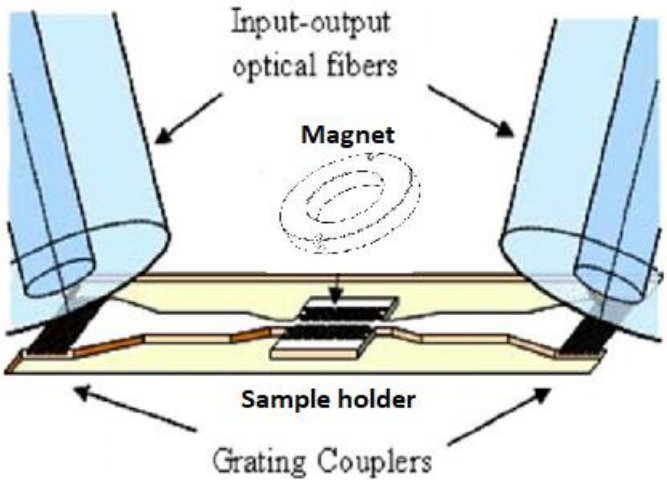

Figure 7.3. Experimental setup used to measure the Faraday rotation of the iron oxide nanoparticles consisting of: Input and output grating couplers, DIYMAG magnet and sample holder.

Figure 7.4 shows the magnetic field of the DIYMAG magnet. The magnetic field spreads out from the south pole, arch around the middle of the magnet and converge again near the north pole. The strength of the force is directly related to the number of lines, as the lines crowd together, the force is strong, where the are spaced widely apart it is weak. This magnetic field lines encompasses the iron oxide nanoparticles deposited on our sample and ensures that we have an adequate magnetic field that will enable the nanoparticles to show rotation.

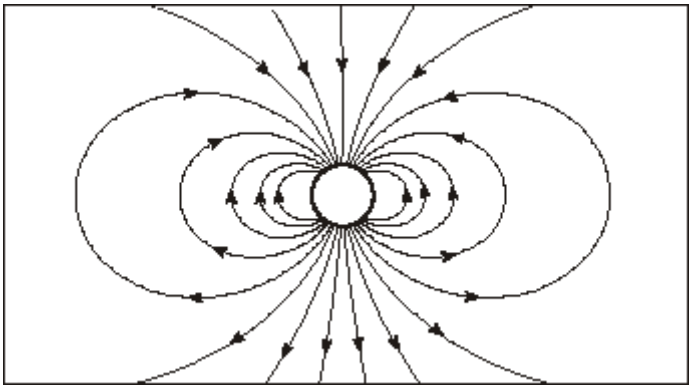

Figure 7.4. Schematic of the magnetic field lines of the DIYMAG magnet.

7.3 Results

For all the chips, iron oxide nanoparticles were spin coated on the silicon substrates. Table 7.1 outlines the polymer used, the loading ratio and annealing condition. The chips are very sensitive to temperature, if the temperature increases above 500°C the chip will be permanently damaged, and the waveguides will be destroyed. The temperatures and time were chosen to yield the most γ – Fe_2O_3 nanoparticles from the two polymers. The two-step low temperature annealing condition used for sample #1 is the annealing conditions proven from chapter 4 to yield the most γ – Fe_2O_3. Moreover, a control sample was used to test how the chips are stressed after plasma etching and the two-step annealing condition.

Table 7.1. Summary of the polymer, loading ratio and annealing conditions used for the four chips tested.

Sample #	Polymer used	Loading ratio	Annealing conditions
1	P4824	0.2	350°C Air 12hrs + 350°C N_2 12hrs
2	P4824	0.2	350°C N_2 2hrs
3	P9861	0.2	350°C N_2 1hrs
Control	N/A	N/A	350°C Air 12hrs + 350°C N_2 12hrs

No nanoparticles were deposited on the control sample, it was meant to test if the stress caused by plasma etching and the two-step annealing process was sufficient to destroy the waveguides. We were able to transmit light through the control sample with no major losses associated to damage done to the chips suggesting that our general approach is sound. For the P9861 sample #3, we expect no optical isolation results from the nanoparticles as the nanoparticles synthesized from P9861 show low magnetic response supported from chapter 4. As expected for sample #3, we did not observe any change in transmission of light.
If successful, we would expect a greater response from sample 1 than sample 2 corresponding to the amount of γ phase in the iron oxide nanoparticles.

Unfortunately, the results for the optical isolation for chips #1 and #2 were disappointing as neither chip showed any response. The iron oxide nanoparticles synthesized by P4824 with a loading ratio of 0.2 should yield γ-phase iron oxide nanoparticles as supported by chapter 4. We expect the two-step temperature annealing at 350°C to have higher magnetization and better Faraday rotation results as a result.

One possible explanation is that the nanoparticles were not quasi-phase matched. Quasi-phase matching (QPM) is a measure of the flow of energy between the TE and TM modes. QPM requires a spatial modulation, as Figure 7.5 shows the accumulated phase difference between the cladding of lengths L_G and L_N. The cladding lengths correspond to the width of the waveguide (L_G), and the distance between the successive waveguides (L_N). The cladding lengths L_G and L_N corresponding respectively to a modal phase offset of $\Delta\phi = 2\pi$ such that we can prevent Faraday rotation where phase relation has the opposite sign for growth and achieve isolation(142). In our case, the nanoparticles might rotate a tiny amount, and then immediately

rotate back which will yield no net Faraday rotation as shown in Figure 7.5 for the modal phase mismatch.

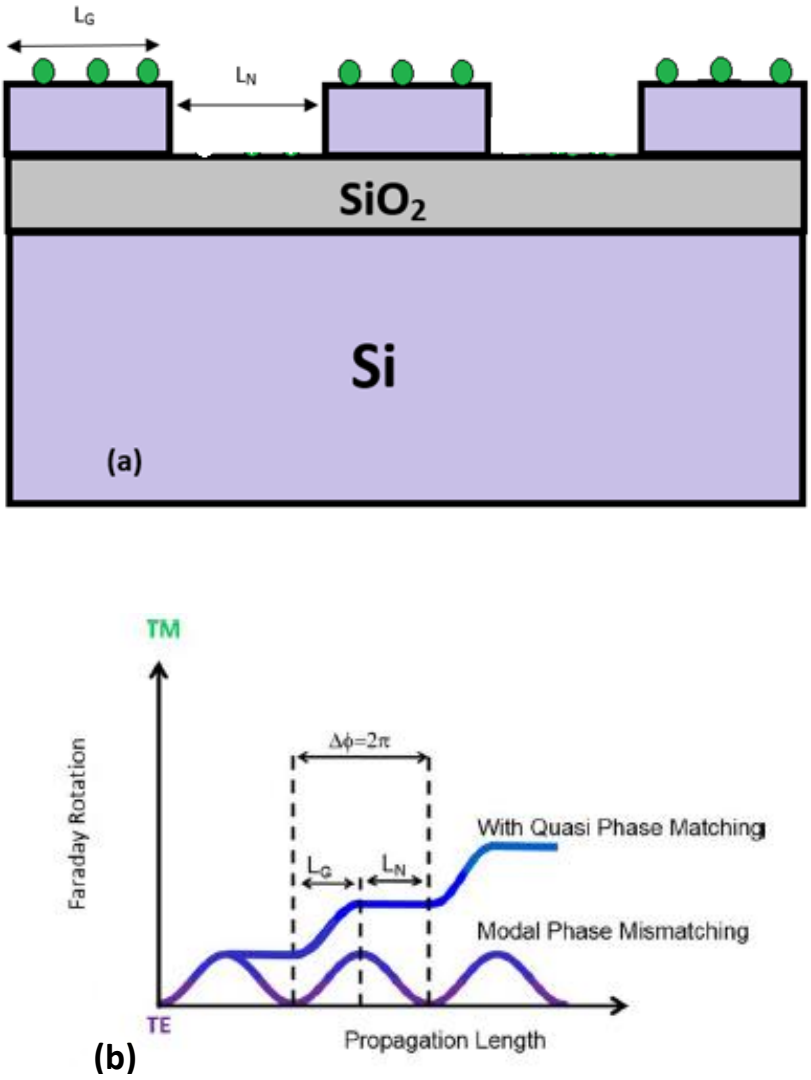

Figure 7.5. (a) Schematic of the components required for a Faraday rotation waveguide isolator with the iron oxide nanoparticles. (b) Schematic showing the effects of phase mismatch and the solution of QPM (143)

QPM could be achieved by calculating the length of the claddings required to have the optimum response from the nanoparticles, then depositing the magnetic nanoparticles only on top of the waveguides. As shown in Fig 7.5(a), using photolithography to coat the sample with the nanoparticles and then use a pre-designed mask to uncover locations where the particles are undesirable followed by a sonication to ensure that the nanoparticles at these specific locations

are gone. This can enable us to have nanoparticles where we require them to be and eliminate other nanoparticles that will contribute to modal phase mismatch.

Moreover, only one wavelength was used to test the iron oxide nanoparticles' response at 1550 nm. More wavelengths could be used to explore the response of the nanoparticles at different wavelengths, particularly in the range from 350 nm to 750 nm as tested by Dani et al. (6), as well as, the near infrared region from 750 nm to 1350 nm.

7.4. Summary

In this chapter, the design and preliminary experimental tests for our proposed optical isolator was shown. We used P4824 and P9861 with a loading ratio of 0.2, the micellular particles were then spun on the silicon chips, etched for 25 minutes and annealed at different annealing conditions. The optical isolation of the nanoparticles was then measured but achieved no response. This is likely due to the modal phase mismatch between the cladding and the nanoparticles. The particles could be quasi-phase matched by using state of the art lithography techniques followed by sonication to eliminate undesirable particles. Finally, a range of wavelengths could be used to test the Faraday rotation of the iron oxide nanoparticles.

Chapter 8

Conclusion and future work

8.1. Summary

The goal for this thesis is to design and fabricate nanoparticles with high magnetization to be used as an optical isolator which can be monolithically integrated with semiconductor lasers used for telecommunications. By using Raman spectra, the iron oxide nanoparticles and tin oxide nanoparticles evolution processes were elucidated in detail in chapters 4 and 5 respectively. The overall process of synthesizing the nanoparticles could be described as:

1) Formation of the PS-b-P2VP reverse micelles
2) Adding $FeCl_3$ precursor for iron oxide nanoparticles or $SnCl_3$ for tin oxide nanoparticles
3) Dispensing (spin coating and drop casting)
4) Oxygen plasma treatment
5) Annealing treatment

Moreover, the magnetic properties of the magnetic nanoparticles arrays were also evaluated by SQUID magnetometer. Chapters 5 and 6 show the difference between iron oxide nanoparticles and tin oxide nanoparticles' magnetization properties. Iron oxide nanoparticles yielding higher percentages of γ-Fe_2O_3 show superior magnetic response than tin oxide nanoparticles. However, more research needs to be done to be able to use tin oxide nanoparticles as optical isolators. For the time being, the best material to use as an optical isolator supported by chapters 5 and 6 is using P4824 with a loading ratio of 0.2 to create iron oxide nanoparticles, followed by a low temperature annealing process at 350°C for 12 hours in Air then another 350°C for 12 hours in N_2. This was proven to show the best magnetic response supported by the Raman and SQUID data and thus, the best material to be used as an optical isolator.

Finally, the iron oxide nanoparticles were spun on the silicon chips, treated with oxygen plasma treatment followed by the low temperature annealing process to test for Optical isolation. However, no optical isolation response was measured from the chips.

8.2. Future work

γ-Fe_2O_3 nanoparticles can be generated with high degree of control in terms of size and dispersion and subsequently the magnetization of the nanoparticles. Incorporating the iron oxide nanoparticles onto silicon chips with quasi phase matching is a good starting point moving forward to investigate the Faraday rotation that the nanoparticles can show. As well as, encapsulating the iron oxide nanoparticles with a gold shell as Dani et al. have done. In addition, tin oxide shows promising results in terms of magnetization compared to the iron oxide nanoparticles. Different annealing times and temperatures could be incorporated for tin oxide nanoparticles in order to yield higher magnetic response, followed by integrating the tin oxide nanoparticles in the same process as iron oxide nanoparticles onto the silicon chips to show signs of optical isolation. In addition, potential future studies could be devoted to exploring the relationship between the dispersion of magnetic nanoparticles and the related magnetic properties. The iron oxide nanoparticles have many potential applications in academia and in the industry as well.

Bibliography

1. Agrawal GP. Optical Communication: Its History and Recent Progress. In: Al-Amri MD, El-Gomati M, Zubairy MS, editors. Optics in Our Time. Cham: Springer International Publishing; 2016.

2. Zaman TR. Integrated Optical Isolators. :129.

3. Cordova BG. Theory and Design of Integrated Optical Isolators and Broadband Couplers Using Fresnel Zone Plates. :114.

4. Amemiya T, Nakano Y. Single Mode Operation of 1.5-µm Waveguide Optical Isolators Based on the Nonreciprocal-loss Phenomenon. In: Young K, editor. Advances in Optical and Photonic Devices. InTech; 2010.

5. Prati E. Propagation in Gyroelectromagnetic Guiding Systems. J Electromagn Waves Appl. 2003 Jan 1;17(8):1177–96.

6. Dani RK, Wang H, Bossmann SH, Wysin G, Chikan V. Faraday rotation enhancement of gold coated Fe_2O_3 nanoparticles: Comparison of experiment and theory. J Chem Phys. 2011 Dec 14;135(22):224502.

7. Gupta AK, Gupta M. Synthesis and Surface Engineering of Iron Oxide Nanoparticles for Biomedical Applications. Biomaterials. 2005;26(18):3995–4021.

8. Laurent S, Forge D, Port M, Roch a, Robic C, Elst LV, et al. Magnetic Iron Oxide Nanoparticles: Synthesis, Stabilization, Vectorization, Physicochemical Characterizations, and Biological Applications. Chem Rev. 2008;108(6):2064–110.

9. Hyeon T. Chemical Synthesis of Magnetic Nanoparticles. Chem Commun. 2003;(8):927–34.

10. Prosini PP, Carewska M, Loreti S, Minarini C, Passerini S. Lithium Iron Oxide as Alternative Anode for Li-Ion Batteries. Int J Inorg Mater. 2000;2(4):365–70.

11. Liong M, Lu J, Kovochich M, Xia T, Ruehm SG, Nel AE, et al. Multifunctional Inorganic Nanoparticles for Imaging, Targeting, and Drug Delivery. ACS Nano. 2008;2(5):889–96.

12. Lee N, Hyeon T. Designed Synthesis of Uniformly Sized Iron Oxide Nanoparticles for Efficient Magnetic Resonance Imaging Contrast Agents. Chem Soc Rev. 2012;41(7):2575–89.

13. Li Z, Wei L, Gao M, Lei H. One-Pot Reaction to Synthesize Biocompatible Magnetite Nanoparticles. Adv Mater. 2005;17(8):1001–5.

14. Bi L, Hu J, Jiang P, Kim DH, Dionne GF, Kimerling LC, et al. On-chip optical isolation in monolithically integrated non-reciprocal optical resonators. Nat Photonics. 2011 Dec;5(12):758–62.

15. Zhu W, Winterstein J, Maimon I, Yin Q, Yuan L, Kolmogorov AN, et al. Atomic Structural Evolution during the Reduction of α-Fe2O3nanowires. J Phys Chem C. 2016 Jul;120(27):14854–62.

16. Cornell RM, Schwertmann U. The iron oxides: structure, properties, reactions, occurrences, and uses. 2nd, completely rev. and extended ed ed. Weinheim: Wiley-VCH; 2003. 664 p.

17. Pati SS, Philip J. Enhancement in maghemite to hematite phase transition temperature with very low fraction of Co (II) doping. In: International Conference on Nanoscience, Engineering and Technology (ICONSET 2011). 2011. p. 323–5.

18. Roca AG, Morales MP, O'Grady K, Serna CJ. Structural and magnetic properties of uniform magnetite nanoparticles prepared by high temperature decomposition of organic precursors. Nanotechnology. 2006 May;17(11):2783–2788.

19. Franco A, e Silva FC. High temperature magnetic properties of cobalt ferrite nanoparticles. Appl Phys Lett. 2010 Apr 26;96(17):172505.

20. Rouquette J, Dolejš D, Kantor IYu, McCammon CA, Frost DJ, Prakapenka VB, et al. Iron-carbon interactions at high temperatures and pressures. Appl Phys Lett. 2008 Mar 24;92(12):121912.

21. Machala L, Tuček J, Zbořil R. Polymorphous Transformations of Nanometric Iron(III) Oxide: A Review. Chem Mater. 2011 Jul;23(14):3255–72.

22. Basina G, Panagiotopoulos I, Devlin E, Hadjipanayis G, Colak L, Hadjipanayis C, et al. Synthesis of Biocompatible Magnetic Iron Oxide (γ-Fe2O3 and Fe3O4) Nanoparticles by a Modified Polyol Process for Biomedical Applications. MRS Proc [Internet]. 2010 Jan [cited 2019 May 2];1256. Available from: http://www.journals.cambridge.org/abstract_S1946427400003444

23. Silva MF, de Oliveira LAS, Ciciliati MA, Lima MK, Ivashita FF, Fernandes de Oliveira DM, et al. The Effects and Role of Polyvinylpyrrolidone on the Size and Phase Composition of Iron Oxide Nanoparticles Prepared by a Modified Sol-Gel Method. Journal of Nanomaterials. 2017.

24. Iida H, Nakanishi T, Takada H, Osaka T. Preparation of magnetic iron-oxide nanoparticles by successive reduction–oxidation in reverse micelles: Effects of reducing agent and atmosphere. Electrochimica Acta. 2006 Oct 5;52(1):292–6.

25. Liang K, Hui LS, Turak A. Probing the multi-step crystallization dynamics of micelle templated nanoparticles: structural evolution of single crystalline γ-Fe $_2$ O $_3$. Nanoscale [Internet]. 2019 [cited 2019 May 2]; Available from: http://xlink.rsc.org/?DOI=C9NR00148D

26. Tai MF, Lai CW, Hamid SBA, Suppiah DD, Lau KS, Yehya WA, et al. Facile synthesis of magnetite iron oxide nanoparticles via precipitation method at different reaction temperatures. Mater Res Innov. 2014 Dec 8;18(sup6):S6-470-S6-473.

27. Sodipo BK, Aziz AA. Sonochemical Synthesis of Silica Coated Super Paramagnetic Iron Oxide Nanoparticles. Materials Science Forum. 2013.

28. Dar MI, Shivashankar SA. Single Crystalline Magnetite, Maghemite, and Hematite Nanoparticles with Rich Coercivity. RSC Adv. 2014;4(8):4105–13.

29. Nuamah RA. SYNTHESIS AND CHARACTERIZATION OF TIN IV OXIDE (SnO2) NANOPARTICLES FOR ENERGY APPLICATIONS. :98.

30. Bhattacharya P, editor. Comprehensive semiconductor science and technology. Amsterdam: Elsevier; 2011.

31. Paraguay-Delgado F, Antúnez-Flores W, Miki-Yoshida M, Aguilar-Elguezabal A, Santiago P, Diaz R, et al. Structural analysis and growing mechanisms for long SnO2nanorods synthesized by spray pyrolysis. Nanotechnology. 2005 Mar;16(6):688–694.

32. Ribeiro C, Lee EJH, Giraldi TR, Aguiar R, Longo E, Leite ER. *In situ* oriented crystal growth in a ceramic nanostructured system. J Appl Phys. 2005 Jan 15;97(2):024313.

33. Liu Y, Koep E, Liu M. A Highly Sensitive and Fast-Responding SnO2 Sensor Fabricated by Combustion Chemical Vapor Deposition. Chem Mater. 2005 Jul 1;17(15):3997–4000.

34. Guan M, Zhao X, Duan L, Cao M, Guo W, Liu J, et al. Controlled synthesis of SnO2 nanostructures with different morphologies and the influence on photocatalysis properties. J Appl Phys. 2013 Sep 16;114(11):114302.

35. Pourfayaz F, Khodadadi A, Mortazavi Y, Mohajerzadeh SS. CeO2 doped SnO2 sensor selective to ethanol in presence of CO, LPG and CH4. Sens Actuators B Chem. 2005;1–2(108):172–6.

36. Moradi L, Ataei Z, Zahraei Z. Convenient synthesis of spirooxindoles using SnO2 nanoparticles as effective reusable catalyst at room temperature and study of their in vitro antimicrobial activity. J Iran Chem Soc [Internet]. 2019 Jan 21 [cited 2019 Mar 7]; Available from: https://doi.org/10.1007/s13738-019-01598-2

37. Chetri P, Choudhury B, Choudhury A. Room temperature ferromagnetism in SnO_2 nanoparticles: an experimental and density functional study. J Mater Chem C. 2014;2(43):9294–302.

38. Kamble VB, Umarji AM. Correlating defect induced ferromagnetism and gas sensing properties of undoped tin oxide sensors. Appl Phys Lett. 2014 Jun 23;104(25):251912.

39. Sabergharesou T, Wang T, Ju L, Radovanovic PV. Electronic structure and magnetic properties of sub-3 nm diameter Mn-doped SnO2 nanocrystals and nanowires. Appl Phys Lett. 2013 Jul 1;103(1):012401.

40. Coey JMD, Douvalis AP, Fitzgerald CB, Venkatesan M. Ferromagnetism in Fe-doped SnO2 thin films. Appl Phys Lett. 2004 Feb 18;84(8):1332–4.

41. Gopinadhan K, Kashyap SC, Pandya DK, Chaudhary S. High temperature ferromagnetism in Mn-doped SnO2 nanocrystalline thin films. J Appl Phys. 2007 Dec 1;102(11):113513.

42. Fu C. Magnetic iron oxide nanoparticles: synthesis, characteristics, magnetic behavior, and biomedical applications. :67.

43. Sundaresan A, Bhargavi R, Rangarajan N, Siddesh U, Rao CNR. Ferromagnetism as a universal feature of nanoparticles of the otherwise nonmagnetic oxides. Phys Rev B [Internet]. 2006 Oct 20 [cited 2019 Feb 24];74(16). Available from: https://link.aps.org/doi/10.1103/PhysRevB.74.161306

44. Zhang L, Ge S, Zuo Y, Zhang B, Xi L. Influence of Oxygen Flow Rate on the Morphology and Magnetism of SnO2 Nanostructures. J Phys Chem C. 2010 May 6;114(17):7541–7.

45. Liheng Wu, Adriana Mendoza-Garcia, Qing Li, and Shouheng Sun. "OrganicPhase Syntheses of Magnetic Nanoparticles and Their Applications.

46. Lu A-H, Salabas EL, Schüth F. Magnetic Nanoparticles: Synthesis, Protection, Functionalization, and Application. Angew Chem Int Ed. 2007;46(8):1222–44.

47. Chetri P, Saikia B, Choudhury A. Structural and optical properties of Cu doped SnO2 nanoparticles: An experimental and density functional study. J Appl Phys. 2013 Jun 21;113(23):233514.

48. Rondinone AJ, Liu C, Zhang ZJ. Determination of Magnetic Anisotropy Distribution and Anisotropy Constant of Manganese Spinel Ferrite Nanoparticles. J Phys Chem B. 2001 Aug;105(33):7967–71.

49. Sung Lee J, Myung Cha J, Young Yoon H, Lee J-K, Keun Kim Y. Magnetic multi-granule nanoclusters: A model system that exhibits universal size effect of magnetic coercivity. Sci Rep [Internet]. 2015 Dec [cited 2019 May 2];5(1). Available from: http://www.nature.com/articles/srep12135

50. Frey NA, Peng S, Cheng K, Sun S. Magnetic nanoparticles: synthesis, functionalization, and applications in bioimaging and magnetic energy storage. Chem Soc Rev. 2009;38(9):2532.

51. Yu HCY, Eijkelenborg MA van, Leon-Saval SG, Argyros A, Barton GW. Enhanced magneto-optical effect in cobalt nanoparticle-doped optical fiber. Appl Opt. 2008 Dec 10;47(35):6497–501.

52. Hayashi K, Fujikawa R, Sakamoto W, Inoue M, Yogo T. Synthesis of Highly Transparent Lithium Ferrite Nanoparticle/Polymer Hybrid Self-standing Films Exhibiting Faraday Rotation in the Visible Region. J Phys Chem C. 2008 Sep 18;112(37):14255–61.

53. Barnakov YA, Scott BL, Golub V, Kelly L, Reddy V, Stokes KL. Spectral dependence of Faraday rotation in magnetite-polymer nanocomposites. J Phys Chem Solids. 2004 May 1;65(5):1005–10.

54. Fujita J, Levy M, Osgood RM, Wilkens L, Dötsch H. Waveguide optical isolator based on Mach–Zehnder interferometer. Appl Phys Lett. 2000 Apr 11;76(16):2158–60.

55. Shimizu H, Tanaka M. Design of semiconductor-waveguide-type optical isolators using the nonreciprocal loss/gain in the magneto-optical waveguides having MnAs nanoclusters. Appl Phys Lett. 2002 Dec 19;81(27):5246–8.

56. Van Parys W, Vanwollenghem M, Van Thourhout D, Baets R, Decobert J, Dagens B, et al. InP-based monolithically integrated optical waveguide isolator with 32 dB/em isolation. In: The 17th Annual Meeting of the IEEELasers and Electro-Optics Society, 2004 LEOS 2004. Rio Grande, Puerto Rico: IEEE; 2004. p. 386–7.

57. Solam A. of the requirements for the degree. :106.

58. Kawano K, Kitoh T. Introduction to Optical Waveguide Analysis [Internet]. New York, USA: John Wiley & Sons, Inc.; 2001 [cited 2019 Jun 10]. Available from: http://doi.wiley.com/10.1002/0471221600

59. Born M, Wolf E. Principles of optics: electromagnetic theory of propagation, interference and diffraction of light. 7th expanded ed. Cambridge ; New York: Cambridge University Press; 1999. 952 p.

60. Classical Electrodynamics, 3rd Edition. Wiley.com.

61. Zayets V. Surface Plasmons.

62. Zayets V, Debnath MC, Ando K. Complete magneto-optical waveguide mode conversion in Cd1−xMnxTe waveguide on GaAs substrate. Appl Phys Lett. 2004 Jan 26;84(4):565–7.

63. Wolfe R, Hegarty J, Dillon JF, Luther LC, Celler GK, Trimble LE, et al. Thin-film waveguide magneto-optic isolator. Appl Phys Lett. 1985 May 1;46(9):817–9.

64. Zaman TR, Guo X, Ram RJ. Faraday rotation in an InP waveguide. Appl Phys Lett. 2007 Jan 8;90(2):023514.

65. Sugimoto N, Terui H, Tate A, Katoh Y, Yamada Y, Sugita A, et al. A hybrid integrated waveguide isolator on a silica-based planar lightwave circuit. J Light Technol. 1996 Nov;14(11):2537–46.

66. Thompson RB, Ginzburg VV, Matsen MW, Balazs AC. Predicting the Mesophases of Copolymer-Nanoparticle Composites. Science. 2001 Jun 29;292(5526):2469–72.

67. Buckingham AD, Stephens PJ. Magnetic Optical Activity. Annu Rev Phys Chem. 1966 Oct 1;17(1):399–432.

68. Talebian E, Talebian M. Experimental study of the Faraday rotation and Verdet constant in nanocrystal and thin films of cadmium manganese telluride samples. Optik. 2015 Dec;126(23):3917–9.

69. Mallet P, Guérin CA, Sentenac A. Maxwell-Garnett mixing rule in the presence of multiple scattering: Derivation and accuracy. Phys Rev B. 2005 Jul 25;72(1):014205.

70. Wang Y, Li Y, Rong C, Liu JP. Sm–Co hard magnetic nanoparticles prepared by surfactant-assisted ball milling. Nanotechnology. 2007 Nov 21;18(46):465701.

71. Binns C. Nanoclusters deposited on surfaces. Surf Sci Rep. 2001 Oct 1;44(1):1–49.

72. Bansmann J, Baker SH, Binns C, Blackman JA, Bucher J-P, Dorantes-Dávila J, et al. Magnetic and structural properties of isolated and assembled clusters. Surf Sci Rep. 2005 Feb 1;56(6):189–275.

73. Edmonds KW, Binns C, Baker SH, Thornton SC, Norris C, Goedkoop JB, et al. Doubling of the orbital magnetic moment in nanoscale Fe clusters. Phys Rev B. 1999 Jul 1;60(1):472–6.

74. Lau JT, Föhlisch A, Nietubyć R, Reif M, Wurth W. Size-Dependent Magnetism of Deposited Small Iron Clusters Studied by X-Ray Magnetic Circular Dichroism. Phys Rev Lett [Internet]. 2002 Jul 15 [cited 2019 Feb 21];89(5). Available from: https://link.aps.org/doi/10.1103/PhysRevLett.89.057201

75. Terheiden A, Rellinghaus B, Stappert S, Acet M, Mayer C. Embedding and self-organization of nanoparticles in phospholipid multilayers. J Chem Phys. 2004 Jun 18;121(1):510–6.

76. Queitsch U, Mohn E, Schäffel F, Schultz L, Rellinghaus B, Blüher A, et al. Regular arrangement of nanoparticles from the gas phase on bacterial surface-protein layers. Appl Phys Lett. 2007 Mar 12;90(11):113114.

77. Sun S. Recent Advances in Chemical Synthesis, Self-Assembly, and Applications of FePt Nanoparticles. Adv Mater. 2006;18(4):393–403.

78. Sun S, Murray CB, Weller D, Folks L, Moser A. Monodisperse FePt Nanoparticles and Ferromagnetic FePt Nanocrystal Superlattices. Science. 2000 Mar 17;287(5460):1989–92.

79. Verdes C, Chantrell RW, Satoh A, Harrell JW, Nikles D. Self-organisation, orientation and magnetic properties of FePt nanoparticle arrays. J Magn Magn Mater. 2006 Sep 1;304(1):27–31.

80. Yang X, Liu C, Ahner J, Yu J, Klemmer T, Johns E, et al. Fabrication of FePt nanoparticles for self-organized magnetic array. J Vac Sci Technol B Microelectron Nanometer Struct Process Meas Phenom. 2003 Dec 24;22(1):31–4.

81. Barick KC, Bahadur D. Self-Assembly of Colloidal Nanoscale Particles: Fabrication, Properties and Applications. 2010.

82. Amiens C, Chaudret B. Organometallic synthesis of nanoparticles. Mod Phys Lett B. 2007 Aug 10;21(18):1133–41.

83. Howard LEM, Nguyen HL, Giblin SR, Tanner BK, Terry I, Hughes AK, et al. A Synthetic Route to Size-Controlled fcc and fct FePt Nanoparticles. J Am Chem Soc. 2005 Jul 1;127(29):10140–1.

84. Cummins C, Ghoshal T, Holmes JD, Morris MA. Strategies for Inorganic Incorporation Using Neat Block Copolymer Thin Films for Etch Mask Function and Nanotechnological Application. Adv Mater. 2016;28(27):5586–618.

85. Förster S, Antonietti M. Amphiphilic Block Copolymers in Structure-Controlled Nanomaterial Hybrids. Adv Mater. 1998;10(3):195–217.

86. Wiedwald U, Han L, Biskupek J, Kaiser U, Ziemann P. Preparation and characterization of supported magnetic nanoparticles prepared by reverse micelles. Beilstein J Nanotechnol. 2010 Nov 22;1:24–47.

87. Shan L, Punniyakoti S, Bael MJV, Temst K, Bael MKV, Ke X, et al. Homopolymers as nanocarriers for the loading of block copolymer micelles with metal salts: a facile way to large-scale ordered arrays of transition-metal nanoparticles. J Mater Chem C. 2013 Dec 19;2(4):701–7.

88. Bütün V, Sönmez Ş, Yarligan S, Taktak FF, Atay A, Bütün S. Micelles and 'reverse micelles' with a novel water-soluble diblock copolymer. Polymer. 2008 Sep 9;49(19):4057–65.

89. Lee S, Kim H, Chae S, Sohn B-H. Diblock copolymer micelles as surface-functionalized particles and direct decoration of nanoparticles on their surface. Polymer. 2015 Mar 20;61:15–9.

90. Hong PP, Boerio FJ, Tirrell M, Dhoot S, Guenoun P. An Investigation of the Adsorption of Polystyrene/Poly (2-Vinylpyridine) Diblock Copolymers onto Silver Substrates Using Surface-Enhanced Raman Scattering. Macromolecules. 1993;26(15):3953–3959.

91. Bennett RD, Miller AC, Kohen NT, Hammond PT, Irvine DJ, Cohen RE. Strategies for Controlling the Planar Arrangement of Block Copolymer Micelles and Inorganic Nanoclusters. Macromolecules. 2005 Dec;38(26):10728–35.

92. Liang K, Eng B. SYNTHESIS AND CHARACTERIZATION OF IRON OXIDE NANOPARTICLES FOR INCORPORATION INTO ORGANIC ELECTRONIC DEVICES. :127.

93. Critical micelle concentration (CMC) and surfactant concentration - KRÜSS. 2018.

94. Mössmer S, Spatz JP, Möller M, Aberle T, Schmidt J, Burchard W. Solution Behavior of Poly(styrene)-block-poly(2-vinylpyridine) Micelles Containing Gold Nanoparticles. Macromolecules. 2000 Jun 1;33(13):4791–8.

95. Yun S-H, Sohn B-H, Jung JC, Zin W-C, Lee J-K, Song O. Tunable Magnetic Arrangement of Iron Oxide Nanoparticles in Situ Synthesized on the Solid Substrate from Diblock Copolymer Micelles. Langmuir. 2005 Jul 1;21(14):6548–52.

96. Yu H. INDIUM TIN OXIDE NANOPARTICLES FORMATION FOR ORGANIC ELECTRONICS. :130.

97. Kumar CSSR, editor. Raman Spectroscopy for Nanomaterials Characterization. Berlin, Heidelberg: Springer Berlin Heidelberg; 2012.

98. Hill PS, Schauble EA. Modeling the effects of bond environment on equilibrium iron isotope fractionation in ferric aquo-chloro complexes. Geochim Cosmochim Acta. 2008 Apr 15;72(8):1939–58.

99. Murata K, Irish DE. Raman studies of the hydrated melt of FeCl36H2O. Spectrochim Acta Part Mol Spectrosc. 1988 Jan 1;44(7):739–43.

100. Yang Y, Qiu T, Liu Z, Hao Q, Lang X, Xu Q, et al. Surface and interference co-enhanced Raman scattering from indium tin oxide nanocap arrays. Appl Surf Sci. 2013 Sep 1;280:343–8.

101. Ding J, Birss VI, Liu G. Formation and Properties of Polystyrene-block-poly(2-cinnamoylethyl methacrylate) Brushes Studied by Surface-Enhanced Raman Scattering and Transmission Electron Microscopy. Macromolecules. 1997 Mar 1;30(5):1442–8.

102. Wiedwald U, Fauth K, Heßler M, Boyen H-G, Weigl F, Hilgendorff M, et al. From Colloidal Co/CoO Core/Shell Nanoparticles to Arrays of Metallic Nanomagnets: Surface Modification and Magnetic Properties. ChemPhysChem. 2005;6(12):2522–6.

103. Russo R, Granata C, Esposito E, Peddis D, Cannas C, Vettoliere A. Nanoparticle magnetization measurements by a high sensitive nano-superconducting quantum interference device. Appl Phys Lett. 2012 Sep 17;101(12):122601.

104. Clarke J. Principles and applications of SQUIDs. Proc IEEE. 1989 Aug;77(8):1208–23.

105. Horcas I, Fernández R, Gómez-Rodríguez JM, Colchero J, Gómez-Herrero J, Baro AM. WSXM: A software for scanning probe microscopy and a tool for nanotechnology. Rev Sci Instrum. 2007 Jan 1;78(1):013705.

106. Hutchings DC, Holmes BM. Quasi-Phase Matching Magneto-Optical Waveguides. MRS Online Proc Libr Arch [Internet]. 2011 ed [cited 2019 Feb 27];1291. Available from: http://www.cambridge.org/core/journals/mrs-online-proceedings-library-archive/article/quasiphase-matching-magnetooptical-waveguides/DC62F88F19718ABFFDED18AC86BFC5B8

107. Horcas I, Fernández R, Gómez-Rodríguez JM, Colchero J, Gómez-Herrero J, Baro AM. WSXM: A software for scanning probe microscopy and a tool for nanotechnology. Rev Sci Instrum. 2007;78(1):013705.

108. Schneider CA, Rasband WS, Eliceiri KW. NIH Image to ImageJ: 25 years of image analysis. Nat Methods. 2012 Jul;9(7):671–5.

109. Boyde A, Mccorkell FA, Taylor GK, Bomphrey RJ, Doube M. Iodine vapor staining for atomic number contrast in backscattered electron and X-ray imaging. Microsc Res Tech. 2014 Dec 1;77(12):1044–51.

110. Liang K, Hui LS, Turak A. Probing the multi-step crystallization dynamics of micelle templated nanoparticles: structural evolution of single crystalline γ-Fe2O3. Nanoscale. 2019 Apr 9;NR-ART-01-2019-000148.

111. Jubb AM, Allen HC. Vibrational Spectroscopic Characterization of Hematite, Maghemite, and Magnetite Thin Films Produced by Vapor Deposition. ACS Appl Mater Interfaces. 2010;2(10):2804–2812.

112. Dar MI, Shivashankar SA. Single crystalline magnetite, maghemite, and hematite nanoparticles with rich coercivity. RSC Adv. 2014;4(8):4105–13.

113. Chourpa I, Douziech-Eyrolles L, Ngaboni-Okassa L, Fouquenet J-F, Cohen-Jonathan S, Soucé M, et al. Molecular Composition of Iron Oxide Nanoparticles, Precursors for Magnetic Drug Targeting, as Characterized by Confocal Raman Microspectroscopy. The Analyst. 2005;130(10):1395.

114. Chamritski I, Burns G. Infrared- and Raman-Active Phonons of Magnetite, Maghemite, and Hematite:\, A Computer Simulation and Spectroscopic Study. J Phys Chem B. 2005 Mar;109(11):4965–8.

115. Bersani D, Lottici PP, Montenero A. Micro-Raman Investigation of Iron Oxide Films and Powders Produced by Sol-Gel Syntheses. J Raman Spectrosc. 1999 May;30(5):355–60.

116. Kanno H, Hiraishi J. A Raman Study of Aqueous Solutions of Ferric Nitrate, Ferrous Chloride and Ferric Chloride in the Glassy State. J Raman Spectrosc. 1982;12(3):224–227.

117. Machala L, Tuček J, Zbořil R. Polymorphous Transformations of Nanometric Iron(III) Oxide: A Review. Chem Mater. 2011 Jul 26;23(14):3255–72.

118. Tsai WH, Boerio FJ, Clarson SJ, Parsonage EE, Tirrell M. Characterization of Adsorbed 2-Vinylpyridine/Styrene Diblock Copolymers on Silver Surfaces Using Surface-Enhanced Raman Scattering. Macromolecules. 1991 Apr;24(9):2538–45.

119. Hong PP, Boerio FJ, Tirrell M, Dhoot S, Guenoun P. An investigation of the adsorption of polystyrene/poly (2-vinylpyridine) diblock copolymers onto silver substrates using surface-enhanced Raman scattering. Macromolecules. 1993;26(15):3953–9.

120. Caswell N, Solin SA. Vibrational Excitations of Pure FeCl3and Graphite Intercalated with Ferric Chloride. Solid State Commun. 1978;27(10):961–7.

121. Zhao W, Tan PH, Liu J, Ferrari AC. Intercalation of Few-Layer Graphite Flakes with FeCl3: Raman Determination of Fermi Level, Layer Decoupling and Stability. J Am Chem Soc. 2011 Apr;133(15):5941–6.

122. de Faria DLA, Venâncio Silva S, de Oliveira MT. Raman Microspectroscopy of Some Iron Oxides and Oxyhydroxides. J Raman Spectrosc. 1997 Nov;28(11):873–8.

123. Zhu H, Deng J, Chen J, Yu R, Xing X. Growth of Hematite Nanowire Arrays during Dense Pentlandite Oxidation. J Mater Chem A. 2014;2(9):3008.

124. Chernyshova IV, Hochella Jr MF, Madden AS. Size-dependent structural transformations of hematite nanoparticles. 1. Phase transition. Phys Chem Chem Phys. 2007;9(14):1736.

125. Jacintho GVM, Corio P, Rubim JC. Surface-Enhanced Raman Spectra of Magnetic Nanoparticles Adsorbed on a Silver Electrode. J Electroanal Chem. 2007;603(1):27–34.

126. Sugimoto T, Muramatsu A. Formation Mechanism of Monodispersed α-Fe2O3Particles in Dilute FeCl3Solutions. J Colloid Interface Sci. 1996 Dec 25;184(2):626–38.

127. Stubenrauch K, Moitzi C, Fritz G, Glatter O, Trimmel G, Stelzer F. Precise Tuning of Micelle, Core, and Shell Size by the Composition of Amphiphilic Block Copolymers Derived from ROMP Investigated by DLS and SAXS. Macromolecules. 2006 Aug 1;39(17):5865–74.

128. Cho Y-H, Yang J-E, Lee J-S. Size control of polymeric nanoparticles from polystyrene-b-poly(2-vinylpyridine). Mater Sci Eng C. 2004 Jan 5;24(1–2):293–5.

129. Zhang L, Eisenberg A. Multiple Morphologies and Characteristics of "Crew-Cut" Micelle-like Aggregates of Polystyrene- *b* -poly(acrylic acid) Diblock Copolymers in Aqueous Solutions. J Am Chem Soc. 1996 Jan;118(13):3168–81.

130. Zhang L, Eisenberg A. Multiple Morphologies of "Crew-Cut" Aggregates of Polystyrene-b-poly(acrylic acid) Block Copolymers. Sci New Ser. 1995;268(5218):1728–31.

131. Yoo SI, Sohn BH, Zin WC, Jung JC, Park C. Mixtures of diblock copolymer micelles by different mixing protocols. Macromolecules. 2007;40(23):8323–8.

132. Reiling S, Besnard M, Bopp PA. Theoretical Studies on the Pyridine−I2 Charge-Transfer Complex. 1. Ab-Initio Calculations on I2 and Pyridine−I2. J Phys Chem A. 1997 Jun 1;101(24):4409–15.

133. Dokukin ME, Sokolov I. Quantitative Mapping of the Elastic Modulus of Soft Materials with HarmoniX and PeakForce QNM AFM Modes. Langmuir. 2012 Nov 20;28(46):16060–71.

134. Young TJ, Monclus MA, Burnett TL, Broughton WR, Ogin SL, Smith PA. The use of the PeakForce TM quantitative nanomechanical mapping AFM-based method for high-resolution Young's modulus measurement of polymers. Meas Sci Technol. 2011;22(12):125703.

135. Hanta G. Determining the Nanomechanical Properties of Micelles [Master of Applied Science]. [Hamilton, Ontario]: McMaster University; 2019.

136. Wang E, Lu J, Bates FS, Lodge TP. Effect of Corona Block Length on the Structure and Chain Exchange Kinetics of Block Copolymer Micelles. Macromolecules. 2018 May 22;51(10):3563–71.

137. Iyama K, Nose T. Kinetics of Micelle Formation with Change of Micelle Shape in a Dilute Solution of Diblock Copolymers. Macromolecules. 1998 Oct 1;31(21):7356–64.

138. Meli L, Santiago JM, Lodge TP. Path-Dependent Morphology and Relaxation Kinetics of Highly Amphiphilic Diblock Copolymer Micelles in Ionic Liquids. Macromolecules. 2010 Feb 23;43(4):2018–27.

139. Smolensky ED, Park H-YE, Zhou Y, Rolla GA, Marjańska M, Botta M, et al. Scaling laws at the nanosize: the effect of particle size and shape on the magnetism and relaxivity of iron oxide nanoparticle contrast agents. J Mater Chem B. 2013;1(22):2818.

140. Baalousha M, Lead JR. Rationalizing Nanomaterial Sizes Measured by Atomic Force Microscopy, Flow Field-Flow Fractionation, and Dynamic Light Scattering: Sample Preparation, Polydispersity, and Particle Structure. Env Sci Technol. 2012 Jun;46(11):6134–6142.

141. Hocini A, Bouras M, Amata H. Theoretical investigations on optical properties of magneto-optical thin film on ion-exchanged glass waveguide. Opt Mater. 2013 Jul;35(9):1669–74.

142. Zhang C, Dulal P, Stadler BJH, Hutchings DC. Monolithically-Integrated TE-mode 1D Silicon-on-Insulator Isolators using Seedlayer-Free Garnet. Sci Rep [Internet]. 2017 Dec [cited 2019 Apr 30];7(1). Available from: http://www.nature.com/articles/s41598-017-06043-z

143. (1) (PDF) Monolithically-Integrated TE-mode 1D Silicon-on-Insulator Isolators using Seedlayer-Free Garnet. ResearchGate.

Acknowledgements

At the end of my thesis, I would like to show my appreciation and gratitude to all the people who have helped, nurtured and supported me during my study at McMaster University for the past two years.

I would like to specifically thank Dr. Knights and Dr. Turak for offering me the opportunity to be a graduate student in their respectable group and giving me academic supervision. Thanks for their supports, suggestions, and discussions.

Many thanks go to the research group of both Dr. Knights and Dr. Turak for their strong support throughout the project. Ramis Arbi, Muhammad Munir, Lok Shu Hui, Kunyu Liang, Gregory Hanta, Dawson Bonneville and David Hagan. Thank you for all the valuable discussions and feedbacks which exert a positive impact on my thesis project. Thanks to Dr. Dube for his help in using SQUID.

I would like to thank the committee members: Dr. Kitai, Dr. Knights, and Dr. Turak for their valued input and for taking the time for my thesis defense.

Finally, I am very grateful to God for providing me with the endless support and encouragement from my parents, brother and fiancée.